Atmos. Chem. Phys., 25, 18617–18637, 2025
https://doi.org/10.5194/acp-25-18617-2025

Atmospheric Chemistry and Physics
Open Access
EGU

An updated microphysical model for particle activation in contrails: the role of volatile plume particles

Joel Ponsonby[1], **Roger Teoh**[1], **Bernd Kärcher**[2], **and Marc E. J. Stettler**[1]

[1]Department of Civil and Environmental Engineering, Imperial College London, London, SW7 2AZ, United Kingdom
[2]Institute for Atmospheric Physics, DLR Oberpfaffenhofen, Weßling, Germany

Correspondence: Marc E. J. Stettler (m.stettler@imperial.ac.uk)

Received: 10 April 2025 – Discussion started: 19 May 2025
Revised: 1 August 2025 – Accepted: 11 August 2025 – Published: 19 December 2025

Abstract. Global simulations suggest the mean annual contrail cirrus net radiative forcing is comparable to that of aviation's accumulated CO_2 emissions. Currently, these simulations assume non-volatile particulate matter (nvPM) and ambient particles are the only source of condensation nuclei, omitting activation of volatile particulate matter (vPM) formed in the nascent plume. Here, we extend a microphysical model to include vPM and benchmark this against a more advanced parcel model (pyrcel) modified to treat contrail formation. We explore how the apparent emission index (EI) of contrail ice crystals (AEI_{ice}) scales with EI_{nvPM}, vPM properties, ambient temperature, and aircraft/fuel characteristics. We find model agreement within 10 %–30 % in the previously defined "soot-poor" regime. However, discrepancies increase non-linearly (up to 60 %) in the "soot-rich" regime, due to differing treatment of droplet growth. Both models predict that, in the "soot-poor" regime, AEI_{ice} approaches 10^{16} kg^{-1} for low ambient temperatures (< 210 K) and sulfur-rich vPM, which is comparable to estimates in the "soot-rich" regime. Moreover, our sensitivity analyses suggest that the point of transition between the "soot-poor" and "soot-rich" regimes is a dynamic threshold that ranges from 10^{13}–10^{16} kg^{-1} and depends sensitively on ambient temperature and vPM properties, underlining the need for vPM emission characterisation measurements. We suggest that existing contrail simulations omitting vPM activation may underestimate AEI_{ice}, especially for flights powered by lean-burn engines. Furthermore, our results imply that, under these conditions, AEI_{ice} might be reduced by (i) reducing fuel sulfur content, (ii) minimising organic emissions, and/or (iii) avoiding cooler regions of the atmosphere.

1 Introduction

The aviation industry contributes approximately 3.5 % towards global anthropogenic effective radiative forcing (ERF) (Lee et al., 2021). This share is projected to increase, as the sector is comparatively challenging to decarbonise (Grewe et al., 2021), notwithstanding anticipated compound annual growth in global passenger traffic of 3.6 % from 2027–2043 (Airbus, 2024). Estimates for 2018 indicate that the largest contribution towards net aviation ERF (+100.9 m Wm^{-2}) is from contrail cirrus (+57.4 m Wm^{-2}), with remaining contributions from accumulated CO_2 emissions (+34.3 m Wm^{-2}), followed by NO_x (+17.5 m Wm^{-2}) (Lee et al., 2021). The sign and magnitude of the contrail cirrus ERF depend inter alia on optical thickness and spatiotemporal coverage (Kärcher, 2018; Schumann et al., 2012), which are determined by ice crystal microphysics and hence the contrail formation pathway.

Provided the aircraft exhaust plume satisfies the Schmidt–Appleman Criterion (SAC), linear contrail formation occurs within 1 s behind the engine exit plane (Schumann, 1996). In the nascent plume, exhaust gases mix with cooler ambient air, resulting in a locally water-supersaturated environment. Under these conditions, particles in the plume can activate to form water droplets, which later nucleate ice homogeneously to form contrail ice crystals. Hence, this pathway is regulated by the number concentration of particles able to activate,

which is controlled by their particle size distribution characteristics and chemical composition (Petters and Kreidenweis, 2007). If fewer particles are able to activate, the resulting ice crystals will be larger and less numerous (Teoh et al., 2022), which may decrease both the optical thickness and the spatiotemporal coverage of the cloud. Therefore, contrail cirrus ERF is inherently sensitive to the characteristics of particles in the mixing plume.

Particles within an exhaust plume are either released by the engine (aircraft mode) or entrained during atmospheric mixing (ambient mode). Aircraft mode particles that evaporate (above) below 350 °C (623 K) (Saffaripour et al., 2020) are defined as (non-)volatile particulate matter, (n)vPM. The largest vPM particles are formed from chemi-ions, which are generated during the combustion process (Yu and Turco, 1997). These chemi-ions scavenge sulfuric acid–water clusters and/or condensable particulate organic matter (POM) in the cooling plume to generate liquid aerosol particles with a number emission index $EI_{vPM} \sim 10^{17}\,kg^{-1}$ (Yu et al., 1998). A smaller, more numerous population of vPM is generated from binary homogeneous nucleation of sulfuric acid and water (Kärcher and Fahey, 1997). However, these particles are efficiently scavenged by the larger particles, enhancing their growth depending on available sulfuric acid and/or POM (Kärcher et al., 2000). They are therefore unlikely to compete with the larger population for plume supersaturations, so we consider the larger population to be plume vPM within this work. The geometric mean diameter (d_g) and hygroscopicity of plume vPM depend on the nature and availability of condensable gases in the aircraft exhaust (Kärcher et al., 2000); $d_{g,vPM}$ is typically < 5 nm (Schumann et al., 2002) prior to contrail formation. Depending on the engine architecture, (semi-)vPM lubrication oil may also be released as larger droplets or gaseous emissions, with the latter capable of either nucleating new particles or contributing towards the condensable organic fraction (Decker et al., 2024; Ungeheuer et al., 2022). By contrast, EI_{nvPM} and $d_{g,nvPM}$ do not change in young exhaust plumes, besides a minor increase to $d_{g,nvPM}$ by accretion of condensable material. Under cruise thrust settings, $d_{g,nvPM} \sim 35$ nm (Durdina et al., 2024) and exhibits dependence on fuel and combustor type (Moore et al., 2017; Voigt et al., 2021).

EI_{nvPM} varies by several orders of magnitude depending on the fuel and engine type (EASA, 2025), with most engines operating in the "soot-rich" regime, where the majority of contrail ice crystals form via nvPM particles (Kärcher and Yu, 2009). Larger nvPM particles ($d_{g,nvPM} > d_{g,vPM}$) activate preferentially in the plume and can suppress water uptake on plume vPM particles, defining "soot-rich" baseline conditions of approximately $EI_{nvPM} > 10^{15}\,kg^{-1}$ (Kärcher, 2018). Upon reducing EI_{nvPM}, size differences no longer compensate for differences in relative abundance, and concentrations of activated nvPM and plume vPM become comparable, characterising the "transition regime" (Kärcher and Yu, 2009). Here, baseline conditions depend sensitively on the characteristics of all particle species. Recent developments in lean-burn technology have been shown to further reduce EI_{nvPM} into the "soot-poor" regime, where activated number concentrations become independent of EI_{nvPM} as EI_{nvPM} decreases. "Soot-poor" baseline conditions have been shown to depend on the relative concentration of ambient particles and the characteristics of plume vPM, including EI_{vPM} and $d_{g,vPM}$ (Yu et al., 2024). Nevertheless, while the role of vPM has been evidenced in model simulations of individual contrails, these effects have not yet been incorporated into global mean contrail cirrus ERF estimates (Bier and Burkhardt, 2022; Teoh et al., 2024).

Generally, two complementary classes of models are used to describe contrail formation (Bier et al., 2022): those that focus on jet dynamics and those that focus on plume microphysics. The former include 3D large eddy simulations (LESs), which provide insight into the spatial heterogeneity within contrail mixing plumes (Lewellen et al., 2014). Inevitably, the high spatial resolution achieved in these simulations is achieved at the expense of detailed microphysical descriptions (Ferreira et al., 2024). To that end, several LES models prescribe water saturation as the critical condition for contrail ice formation (Paoli et al., 2013; Picot et al., 2015) or heterogeneous ice nucleation as the primary formation pathway (Khou et al., 2017, 2015), both of which have been rejected by in situ observations (Kärcher et al., 2015). More representative microphysical treatment can be achieved using 0D box- and parcel model simulations (Bier et al., 2022; Rojo et al., 2015; Yu et al., 2024). Here, the dilution of a parcel of exhaust air is simulated, and microphysical phase transitions, such as particle activation and homogeneous ice nucleation, are tracked. While these models are unable to incorporate feedback between different plume parcels, which may otherwise lead to a diversity of particle history (Lewellen, 2020), they are configured for sophisticated treatment of complex ice microphysics, which is critical for describing contrail properties (Yu et al., 2024).

Here, we undertake a literature review of the microphysical pathway to contrail formation, to better understand the role of plume vPM in contrail formation. We then extend two parcel models using detailed microphysics to account for the activation of plume vPM. In both models, we prescribe plume vPM properties at the time of droplet formation and ice nucleation (0.1–1 s after emission) rather than explicitly modelling their formation. The two models include (i) a minimal microphysical framework developed by Kärcher et al. (2015), henceforth referred to using the shorthand K15, and (ii) a more complex numerical parcel model (pyrcel) developed by Rothenberg and Wang (Rothenberg and Wang, 2016). The extended K15 model is designed for future integration into global contrail simulations, while the modified pyrcel model serves as a benchmark to highlight model discrepancies. After examining these discrepancies, we use the modified pyrcel model to perform a suite of sensitivity analyses, studying the influence of the prescribed vPM size dis-

tribution characteristics and hygroscopicity, ambient temperature, and aircraft/fuel properties.

In Sect. 2, we provide an overview of elementary contrail thermodynamics (Sect. 2.1), a description of particle activation in contrail mixing plumes (Sect. 2.2), and implications for the SAC (Sect. 2.3). Next, we provide an overview of the underlying model framework (Sect. 3.1) and extensions (Sect. 3.2 and 3.3) and of the assumed particle characteristics used in this work (Sect. 3.4). We then evaluate the two models in Sect. 4.1 and 4.2, justifying the use of the modified pyrcel model for several sensitivity analyses (Sect. 4.3–4.6). Finally, we comment on several implications for future modelling studies and wider impacts (Sect. 5).

2 Background

Here, we review the thermodynamic pathway to contrail formation and define the SAC framework (Sect. 2.1). We describe several fundamental principles of particle activation (Sect. 2.2) and use these to justify an extension to the original SAC framework (Sect. 2.3). Finally, we provide a theoretical framework for the parcel models used within this work (Sect. 2.4).

2.1 Thermodynamics of contrail formation

A cruising aircraft releases combustion emissions at a typical engine exhaust temperature $T_E \sim 600\,K$, which depends on the engine architecture and bypass ratio (Cumpsty, 2003). The emissions are dispersed into the turbulent jet plume of the aircraft and are rapidly diluted by upper-tropospheric air, cooling to the ambient temperature (T_A) within 1 s. We can use the partial pressure of water in the mixing plume ($p_{v,M}$) to navigate the transition between exhaust and ambient conditions. For isobaric conditions, this property scales linearly between exhaust and ambient conditions (Rogers and Yau, 1996):

$$G = \frac{\mathrm{d}p_{v,M}}{\mathrm{d}T} = \frac{p_{v,E} - p_{v,A}}{T_E - T_A}, \tag{1}$$

where $p_{v,E}$ and $p_{v,A}$ represent the partial pressure of water in the exhaust and ambient air, respectively, and G is the gradient of the mixing line. Provided we know the ambient conditions ($p_{v,A}$, T_A) and T_E, to fully constrain Eq. (1), we must also define either $p_{v,E}$ or G. Conveniently, the latter has been shown to depend on the aircraft and fuel properties (Schumann, 1996):

$$G = \frac{c_p \mathrm{EI}_w P_T}{\varepsilon Q(1-\eta)}, \tag{2}$$

where P_T is the ambient air pressure, c_p is the isobaric specific heat of air ($1004\,J\,kg^{-1}$), EI_w is the mass emission index of water vapour, ε is the ratio of gas constants for water vapour and dry air (0.622), and η is the overall efficiency such that $(1–\eta)$ represents the fraction of the total heat released per mass of fuel burned (Q) that is transferred to the exhaust gas. We can describe $p_{v,M}$ by re-arranging Eq. (1):

$$p_{v,M} = p_{v,A} + G(T - T_A). \tag{3}$$

Often, it is useful to describe how the water or ice saturation ratio of the plume ($S_{v,M}$ and $S_{i,M}$, respectively) evolves during the mixing process (Fig. 1). Here, we define $S_{v,M}$ and $S_{i,M}$ within the mixing plume as follows:

$$S_{v,M} = \frac{p_{v,M}}{p_{liq}(T)}, \tag{4}$$

$$S_{i,M} = \frac{p_{v,M}}{p_{ice}(T)}. \tag{5}$$

$p_{liq}(T)$ and $p_{ice}(T)$ represent the saturation vapour pressure above a plane surface of supercooled liquid water or ice, respectively (Murphy and Koop, 2005). In turn, we use Eq. (4) to define the liquid water supersaturation within the contrail mixing plume as $s_{v,M} = S_{v,M} - 1$.

To illustrate several features associated with contrail formation, we have shown an example of mixing behaviour for typical aircraft and fuel properties; see Fig. 1. The first feature is the crux of the SAC: contrail formation can only occur if $S_{v,M} > 1$ ($s_{v,M} > 0$). However, this represents only an approximate requirement for the activation of particles into liquid droplets, which we will discuss further in Sect. 2.2 and 2.3. Nevertheless, as originally defined, the SAC may be interpreted quantitatively as

$$\left.\frac{\mathrm{d}p_{liq}(T)}{\mathrm{d}T}\right|_{\theta_G} = G, \tag{6}$$

where θ_G is the temperature at which the contrail mixing line tangentially intersects p_{liq}. Under this definition, θ_G represents the highest temperature at which contrail formation can occur in a water-saturated plume. For ambient relative humidities below water saturation ($p_{v,A} < p_{liq}$), this corresponds to a projected ambient temperature known as the Schmidt–Appleman threshold temperature (T_{SAC}) (Schumann et al., 1996). Accordingly, T_{SAC} represents the highest *ambient* temperature at which contrail formation can occur. The mixing behaviour presented in Fig. 1 is consistent with this threshold condition. Notably, for lower T_A and fixed $p_{v,A}$, the mixing line would be translated towards cooler T by an amount ΔT_{SAC}, and the plume would become supersaturated during mixing. Hence, the parameter ΔT_{SAC} provides a useful indicator for the degree of supersaturation experienced by a contrail mixing plume. Importantly, the SAC implies that the activation of particles into liquid droplets occurs before ice nucleation takes place.

This water saturation constraint is consistent with observations of young contrails (Kärcher et al., 2015) and implies a formation pathway of condensation followed by homogeneous ice nucleation (Murray et al., 2012). As such,

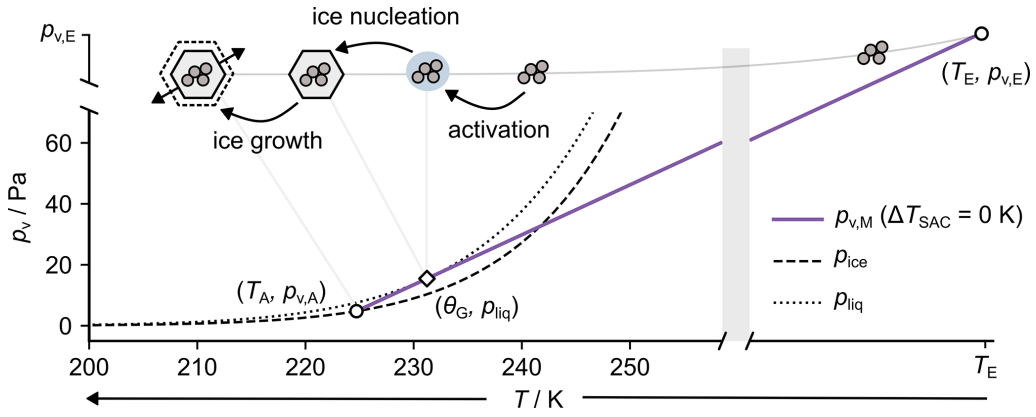

Figure 1. Partial pressure of water vapour (p_v) and temperature of the plume (T) during contrail mixing (purple line) under threshold conditions ($T_A = T_{SAC}$). Saturation vapour pressures above ice (p_{ice}) and water (p_{liq}) are also shown. Finally, a schematic representation of particle emission, activation, and ice nucleation is shown. The latter two occur simultaneously within the original SAC framework. Here, we assume typical aircraft and fuel properties of P_T, EI_w, Q, and η of 25 kPa, 1.23 kg kg^{-1}, 43.2 MJ, and 0.3 for temperatures T_A and T_E of $\sim$ 224 and 600 K, respectively.

we omit heterogeneous ice nucleation in our analysis, which would otherwise contradict this mechanism. The water saturation constraint is also motivated by particle properties because (a) aircraft-emitted nvPM particles have previously been shown as inactive heterogeneous ice nuclei (Testa et al., 2024); (b) only a small subset of ambient tropospheric aerosol particles (mineral dust, ammonium sulfate, and amorphous organic) are efficient heterogeneous ice nuclei (Kärcher et al., 2023), and these have low number concentrations at cruise altitudes (relative to lean-burn EI_{nvPM}); and (c) plume vPM is likely to be at least partly soluble and therefore inactive as heterogeneous ice nuclei. Therefore, in the context of nvPM, the water saturation constraint implies that particles first activate to form water droplets, after which they act as passive inclusions, with rates of homogeneous ice nucleation controlled by the ambient temperature and volume of adsorbed water. In the context of plume vPM and ambient particles, we extend this analysis and demonstrate that the process of ice formation is again strictly sequential, with particle activation occurring before homogeneous ice nucleation; see Sect. S1 in the Supplement. For this reason, contrail formation is dictated by the conditions under which particle activation takes place, which are addressed in Sect. 2.2.

2.2 Aerosol particle activation and the κ–Köhler framework

The equilibrium saturation ratio over a particle may be described as a balance of two interactions (Seinfeld and Pandis, 2016). The first of these is the Kelvin (also commonly referred to as the "surface curvature") effect. Consider the situation whereby a particle with a (dry-particle) diameter d_d is activated to form a pure liquid droplet with a (wet-particle) diameter of d_w. Due to surface tension at the water–air interface, a decrease in the droplet diameter leads to an increase in the partial pressure of water vapour at the droplet surface and hence to an increase in the water saturation ratio (S_v). This effect is parameterised as

$$S_v = a_w e^{\left(\frac{4\sigma_s M_w}{RT\rho_w d_w}\right)}, \tag{7}$$

where σ_s is the surface tension of the liquid–air interface, M_w is the molar mass of water, ρ_w is the density of the liquid, R is the global gas constant, T is the temperature, and a_w is the activity of water in solution (Petters and Kreidenweis, 2007). For particles that are entirely insoluble, the liquid surrounding the particle will be pure water, and we can approximate $a_w = 1$, reducing Eq. (7) to the Kelvin equation (Pruppacher and Klett, 2010). This simplified treatment of insoluble particle activation has been revisited by several studies that consider multilayer adsorption mechanisms (Kumar et al., 2009; Sorjamaa and Laaksonen, 2007), although the application of these approaches is limited by the availability of experimental data. In contrast, if the particle is not entirely insoluble (for example, the insoluble core may contain a soluble coating), the value of a_w (and S_v) is reduced, thus defining the second, solute effect. In this case, the activity of water in solution may be treated using the parameterisation proposed by Petters and Kreidenweis (2007). Here, the particle is described using a hygroscopicity parameter (κ), which is related to the bulk material solubility (Sullivan et al., 2009), and a_w is given by

$$a_w = \frac{d_w^3 - d_d^3}{d_w^3 - d_d^3(1-\kappa)}, \tag{8}$$

where, for an internally mixed particle, κ is given as a volume-weighted sum over the individual components. Note that Eq. (7) collapses to $a_w = 1$ if $\kappa = 0$, which is the approximate limit for a non-hygroscopic (insoluble) particle. Above

this limit, κ is typically represented on a logarithmic scale, with slightly hygroscopic materials ($\kappa < 0.01$) less capable of water uptake than very hygroscopic materials ($\kappa > 0.5$) (Petters and Kreidenweis, 2007). Combining Eqs. (7) and (8), we recover the final form of κ-Köhler theory,

$$S_v = \frac{d_w^3 - d_d^3}{d_w^3 - d_d^3(1-\kappa)} e^{\left(\frac{4\sigma_s M_w}{RT\rho_w d_w}\right)}. \quad (9)$$

According to Eq. (9), S_v increases with d_w up to a maximum at ($d_{w,c}$, $S_{v,c}$), beyond which it declines; see Fig. 2a. These critical parameters may be estimated for a given particle type and at a given T by setting the derivative of Eq. (9) equal to zero and solving numerically. In the context of particle activation, it is more instructive to explore how d_w depends on the ambient saturation ratio, remaining mindful that the inverse function $d_w = d_w(S_v)$ is multivalued. To that end, as the ambient S_v is increased over a particle, growth is initially regulated by the solute effect, and the particle diameter increases by slow, hygroscopic growth. Upon further increasing S_v, the relative magnitudes of the Kelvin and solute effects balance at the critical point ($S_{v,c}, d_{w,c}$) (Seinfeld and Pandis, 2016). Here, the particle is said to have been activated, and subsequent growth is regulated by kinetic droplet growth outlined in Sect. S2. In summary, a particle is considered activated to form a water droplet once the ambient S_v exceeds $S_{v,c}$.

Figure 2b shows that $S_{v,c}$ exhibits three key trends: (i) it increases with both d_d and κ; (ii) it is more sensitive to changes in d_d than κ (i.e. $\frac{dS_{v,c}}{dd_d} \gg \frac{dS_{v,c}}{d\kappa}$); and (iii) it approaches 1 in the limit $(\kappa, d_p) \to (1, \infty)$, $S_{v,c} \to 1$, for which additional justification is provided in Sect. S3. In Fig. 2b, we also show how $S_{v,c}$ varies for a series of mixed particles with insoluble ($\kappa = 0$) cores and variable coatings of hygroscopic ($\kappa = 1$) material (0.5 wt %–50 wt %) with similar total dry-particle diameters $d_d = 10$ nm. These highlight the importance of soluble coatings when considering plume particle activation, which is a feature we return to in Sect. 4.5.

2.3 Extended Schmidt–Appleman framework

As discussed in Sect. 2.1, the SAC assumes that contrails are formed if the mixing line becomes (super)saturated with respect to water during plume evolution ($S_v \geq 1$). However, as outlined in Sect. S3, this criterion cannot be reconciled with the minimum requirement for (even hygroscopic) particle activation.

Instead, suppose that a contrail mixing contains a single particle mode with properties (d_d, κ). Now, the criterion for contrail formation is that the contrail mixing line must contact $p_{liq} \cdot S_{v,c}(T, d_d, \kappa)$ at least once during the mixing process. Figure 3a shows that, when these particle properties are included, the threshold requirement for activation (previously water-saturated conditions, dotted black line) is elevated (grey/green dotted line). Using Eq. (9), the particle dependence of $\Delta T_{SAC} = \Delta T_{SAC}(T, d_d, \kappa)$ can be determined and is shown in Fig. 3b. Alternatively, we can reframe the parameter $\Delta T_{SAC}(T, d_d, \kappa)$ presented in Fig. 3b to be an *effective* Schmidt–Appleman temperature, $T_{SAC}(d_d, \kappa)$, the ambient temperature below which contrail formation takes place when the plume contains particles with properties d_d and κ. Figure 3b also enables us to estimate for which particle types the SAC framework (as outlined in Sect. 2.1) remains applicable, under a specified temperature uncertainty.

For particles with $\kappa > 0.6$ and/or $d_d > 20$ nm, $\Delta T_{SAC}(T, d_d, \kappa) < 2$ K, which is close to the typical uncertainty associated with low-altitude temperature measurements during in situ campaigns, $\Delta T = \pm 1.9$ K (Bräuer et al., 2021). Therefore, for "soot-rich" emissions, where the typical nvPM particles have $d_d > 20$ nm, the condition for applying the original SAC is valid within measurement uncertainty. This explains the success of this approach over the past decades and across various measurement campaigns (Schumann et al., 2017). However, with reduced soot emissions, exhaust material will be enriched with smaller plume vPM particles. Under these circumstances, the SAC is less effective at predicting the temperature at which *most particles* activate; see Fig. 3b.

3 Model

Here, we outline the fundamental relations used to describe a parcel model for contrail formation (Sect. 3.1), including a basic overview of the original K15 model. Next, we outline several extensions made to the K15 model so that it can be applied to treat plume vPM activation (Sect. 3.2). Then, we outline modifications made to a pre-existing cloud parcel model, pyrcel (Rothenberg and Wang, 2016), to simulate the early stages of contrail formation (Sect. 3.3). Finally, we describe the parameter space used in our model simulations (Sect. 3.4).

3.1 Contrail parcel model

As discussed in Sect. 2.2, the critical parameter governing the uptake of water onto particles is the water saturation ratio, S_v. The water saturation ratio within a parcel of air can be described as

$$S_v = \frac{P_T}{p_{liq}(\varepsilon + w_v)} w_v, \quad (10)$$

where ε (= 0.622) is the ratio of the molar mass of water (18.02 g mol^{-1}) to the molar mass of dry air (28.97 g mol^{-1}) and w_v is the water vapour mixing ratio, the mass of water vapour per unit mass of dry air contained within the parcel. We can simplify Eq. (10) further using several features of contrail mixing. Within a contrail, the maximum partial pressure of water vapour in the plume is given by the maximum of $S_v \cdot p_{liq}$. This is bounded by $S_{v,M} \cdot p_{liq}$, since isobaric mixing is the only process that acts to increase the

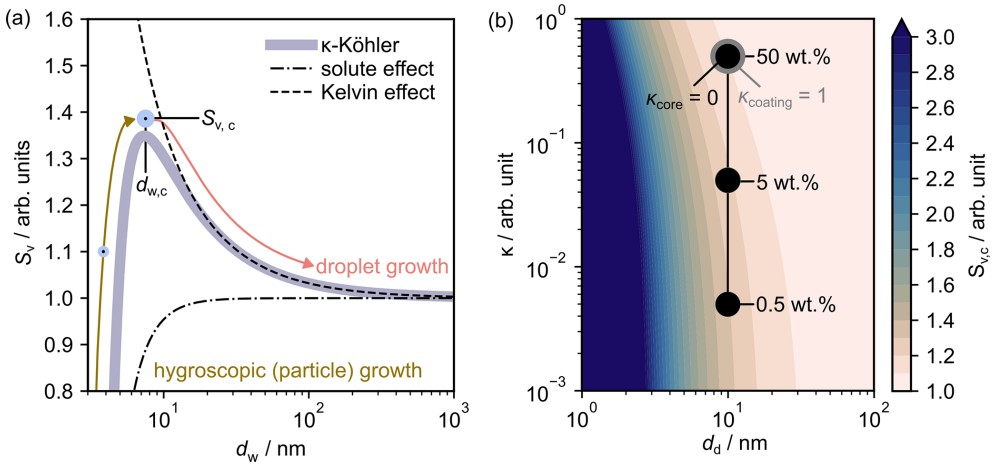

Figure 2. **(a)** Water saturation ratio (S_v) with increasing wet-particle diameter (d_w) as the combination of the solute and Kelvin effects. The critical diameter ($d_{w,c}$) and the associated critical saturation ratio ($S_{v,c}$) mark the point at which a particle is considered activated. **(b)** $S_{v,c}$ is shown as a function of the dry-particle diameter (d_d) and particle hygroscopicity. Values for insoluble ($\kappa = 0$) particles with variable highly soluble ($\kappa = 1$) coatings have been shown for reference.

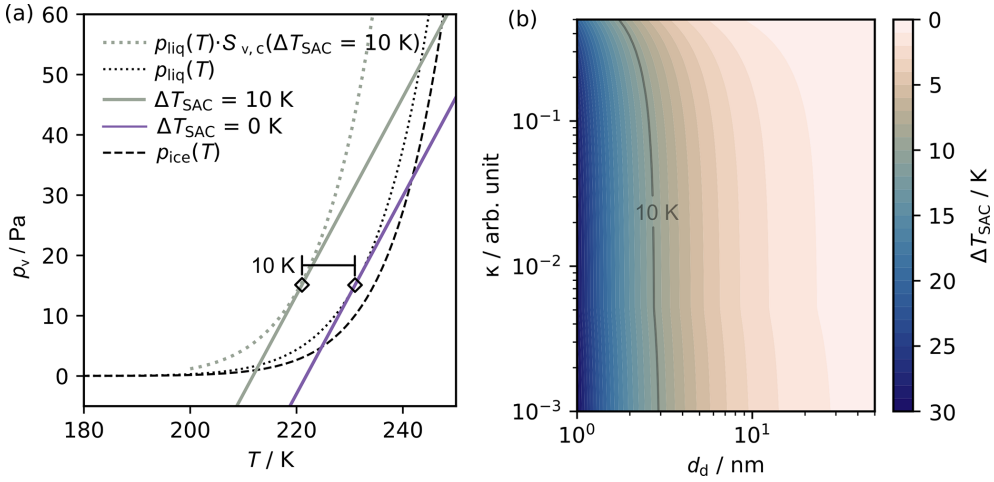

Figure 3. **(a)** Saturation vapour pressure above water (p_{liq}) (purple, dotted) and a contrail mixing line (purple, solid) for threshold conditions, $\Delta T_{SAC} = 0$ K. Particle properties (d_d, κ) have been chosen so that the modified saturation vapour pressure above water $p_{liq} \cdot S_{v,c}$ (d_d, κ) (grey/green, dotted) translates threshold conditions by 10 K, so $\Delta T_{SAC} = 10$ K (grey/green, solid). **(b)** Extension of panel **(a)** to show dependence of ΔT_{SAC} on d_d and κ. Combinations of particle properties resulting in $\Delta T_{SAC} = 10$ K are shown (grey/green, solid). In all cases, $S_{v,c}$ is estimated conservatively using $T = 220$ K.

parcel saturation ratio. Assuming that the ambient environment is ice-saturated, we also know that $p_{v,M}$ is bounded by $(p_{v,M})_{max} = p_{ice}(T_A) + G \cdot (T_E - T_A)$, provided we prescribe an anomalously-low T_A of 200 K. Rearranging Eq. (10), we can therefore bound w_v as

$$w_v < \frac{\varepsilon (p_{v,M})_{max}}{P_T - (p_{v,M})_{max}}. \tag{11}$$

Using $T_E = 600$ K, $T_{SAC} = 224$ K, $G = 1.64\,\mathrm{Pa\,K^{-1}}$, and $P_T = 23\,000$ Pa, we have $w_v < 0.02$. Therefore, the inequality $w_v \ll \varepsilon$ is satisfied for all conditions, which enables us to simplify Eq. (10) as

$$S_v = \frac{P_T}{p_{liq}\varepsilon} w_v. \tag{12}$$

Next, we assume that contrail mixing occurs at constant atmospheric pressure so that, upon differentiating Eq. (12) with respect to time and collecting like terms, we have

$$\frac{dS_v}{dt} = \frac{P_d T}{p_{liq}\varepsilon}\frac{dw_v}{dt} - S_v \frac{1}{p_{liq}}\frac{dp_{liq}}{dt}, \tag{13}$$

$$\frac{dw_v}{dt} = -\left(\frac{dw_c}{dt}\right)_{microphysical} + \left(\frac{dw_{v,M}}{dt}\right)_{mixing}. \tag{14}$$

Equation (14) is a statement of mass conservation: any change in the water vapour content of the parcel must result either from particle microphysical processes (i.e. particle activation and droplet/ice crystal growth) or from plume mixing vapour. Using Eq. (10), we can express the mixing term as

$$\left(\frac{\mathrm{d}w_{\mathrm{v,M}}}{\mathrm{d}t}\right)_{\mathrm{mixing}} = \dot{T}\frac{\mathrm{d}}{\mathrm{d}T}\left(\frac{\varepsilon p_{\mathrm{v,M}}}{P_T}\right) = \frac{\varepsilon}{P_T}G\dot{T}, \tag{15}$$

where $\dot{T}$ is the cooling rate in the plume. Then, combining Eqs. (12)–(15), we arrive at the governing equation

$$\frac{\mathrm{d}S_{\mathrm{v}}}{\mathrm{d}t} = \frac{1}{p_{\mathrm{liq}}}G\dot{T} - S_{\mathrm{v}}\frac{1}{p_{\mathrm{liq}}}\frac{\mathrm{d}p_{\mathrm{liq}}}{\mathrm{d}t} - \frac{P_T}{p_{\mathrm{liq}}\varepsilon}\frac{\mathrm{d}w_{\mathrm{c}}}{\mathrm{d}t}. \tag{16}$$

This is almost identical to the result given by Kärcher et al. (2015). However, we find that, on the right-hand side of Eq. (16), the actual plume saturation ratio (S_{v}) is present rather than the saturation ratio assumed from mixing alone ($S_{\mathrm{v,M}}$). This equation can be solved numerically, for example, by using a numerical parcel model. However, the equation cannot be solved analytically. Under these circumstances, a solution may be derived by firstly approximating $S_{\mathrm{v}} \sim S_{\mathrm{v,M}}$ on the right-hand side of Eq. (16) as in the original K15 model, which effectively decouples the equation. In this purely analytical case, we can generalise Eq. (16) in the form

$$\frac{\mathrm{d}S_{\mathrm{v}}}{\mathrm{d}t} = P_{\mathrm{w}} - L_{\mathrm{w}}, \tag{17}$$

where P_{w} represents the rate of change of the water saturation ratio without particles in the plume and L_{w} represents the rate of change of the water saturation ratio resulting from (a) particle activation to form water droplets and (b) the growth of droplets and/or ice crystals. The description for P_{w} follows from the description of contrail mixing outlined in Sect. 2.1 and is given by Kärcher et al. (2015):

$$P_{\mathrm{w}} = \frac{1}{p_{\mathrm{liq}}}G\dot{T} - S_{\mathrm{v,M}}\frac{1}{p_{\mathrm{liq}}}\frac{\mathrm{d}p_{\mathrm{liq}}}{\mathrm{d}t} = \frac{\mathrm{d}S_{\mathrm{v,M}}}{\mathrm{d}t}. \tag{18}$$

Using the description of mixing provided by Kärcher et al. (2015), next we will outline the equations necessary to estimate the cooling rate. For a full description of the parameters and underlying approximations, the reader is directed to the original text and references therein. The contrail mixing plume cools as it is diluted with ambient air according to the dilution factor

$$D(T) = \frac{T - T_{\mathrm{A}}}{T_{\mathrm{E}} - T_{\mathrm{A}}}, \tag{19}$$

which describes how the cross-sectional area of the plume decreases with decreasing ambient temperature. The temporal evolution of the plume is then described by

$$\frac{\mathrm{d}T}{\mathrm{d}t} = -\beta\frac{T_{\mathrm{E}} - T_{\mathrm{A}}}{\tau_{\mathrm{m}}}D^{1+1/\beta}, \tag{20}$$

$$t = \tau_{\mathrm{m}}D^{-1/\beta}, \tag{21}$$

where τ_{m} is the timescale over which the contrail mixing parcel is unaffected by entrainment and β is a constant dilution parameter. Note that we choose to omit effects associated with latent heat within our simulations, which we found to have a negligible impact on projected ice crystal number concentrations. Therefore, if we have knowledge of the aircraft and ambient conditions, using Eqs. (19)–(21), we are now able to describe P_{w} within the contrail mixing parcel at a given temperature. These relations also govern particle dilution within the cooling contrail mixing parcel. To that end, the total particle number concentration of aircraft (n_{T}) and ambient ($n_{\mathrm{a,T}}$) particle modes are, respectively,

$$n_{\mathrm{T}} = \frac{D(T)\rho_{\mathrm{a}}(T)}{N_0}\mathrm{EI}, \tag{22}$$

$$n_{\mathrm{a},T} = \frac{T_{\mathrm{A}}}{T}[1 - D(T)]n_{\mathrm{a},0}, \tag{23}$$

where ρ_{a} is the mass density of ambient air, EI represents the emission index of the aircraft mode, $n_{\mathrm{a},0}$ represents the ambient number concentration far from the plume, and N_0 is the mass-based mixing ratio according to the K15 model. Particle types are assumed to conform to lognormal particle size distributions and described using a fixed (total) hygroscopicity parameter, κ. For this reason, only a fraction of the total particles within a given mode will be able to activate under a given set of ambient conditions. The activated number concentration can be estimated by integrating over the particle size distribution using Eq. (9), using a methodology outlined in Sect. S4. The second term in Eq. (17), L_{w}, may be expressed as in Korolev and Mazin (2003):

$$L_{\mathrm{w}} = \frac{P_{\mathrm{T}}}{p_{\mathrm{liq}}\varepsilon}\frac{\mathrm{d}w_{\mathrm{c}}}{\mathrm{d}t};\ \frac{\mathrm{d}w_{\mathrm{c}}}{\mathrm{d}t} = \frac{4\pi\rho_{\mathrm{w}}}{\rho_{\mathrm{a}}}\sum_{i=1}^{n} n_{\mathrm{w,i}}r_{\mathrm{w,i}}^2\dot{r}_{\mathrm{w,i}}, \tag{24}$$

where $n_{\mathrm{w,i}}$ is the number concentration of droplets, $r_{\mathrm{w,i}}$ is the droplet radius, and $\dot{r}_{\mathrm{w,i}}$ is the droplet growth rate of these droplets; see Sect. S2. In Eq. (24), we summed contributions from each of the droplets at a given time t. Another useful formulation of Eq. (24) is

$$L_{\mathrm{w}} = \frac{P_{\mathrm{T}}}{p_{\mathrm{liq}}\varepsilon}\frac{4\pi\rho_{\mathrm{w}}}{\rho_{\mathrm{a}}}\int_0^{\infty}\mathrm{d}r_0\frac{\mathrm{d}n_{\mathrm{w}}}{\mathrm{d}r_0}\int_{-\infty}^{t}\dot{n}_{\mathrm{w}}(t_0)r_{\mathrm{w}}^2(t,t_0)\,\dot{r}_{\mathrm{w}}(t,t_0)\,\mathrm{d}t_0, \tag{25}$$

where $\dot{n}_{\mathrm{w}}(t_0)\mathrm{d}t_0$ is the number density of aerosol particles that activate between times t_0 and $t + \mathrm{d}t_0$, $4\pi r_{\mathrm{w}}^2(t,t_0)$ is related to the volumetric flux of water towards water droplets at time t that first formed at time $t_0 < t$, and $\dot{r}_{\mathrm{w}}(t,t_0)$ is the growth rate of these droplets at time t (Kärcher and Lohmann, 2002a). We also integrated over the size distribution of activated particles, $\frac{\mathrm{d}n_{\mathrm{w}}}{\mathrm{d}r_0}$. In Eq. (25), rather than summing over contributions from each droplet at a given time t, we have instead integrated over each time $t_0 < t$ and estimated the projected contribution towards the final time t. Equations (24) and (25) are therefore equivalent representations that are suited to different applications.

Finally, the contrail mixing behaviour can be described using P_w in combination with either expression for L_w. The formulation in Eq. (24) is used in traditional cloud parcel models using discretised particle and droplet size distributions, which enables Eq. (17) to be solved iteratively as a function of time. This forms the basis for the pyrcel model, which is described in more detail in Sect. 3.3. On the other hand, in the K15 model, the formulation in Eq. (25) is solved analytically at each time step, assuming that particle activation and droplet growth at time $t < t_0$ do not affect S_v at time t_0. At each time t, we estimate the critical droplet number concentration required to prevent any further change in the plume saturation ratio $\left(\frac{dS_v}{dt} = 0\right)$. Using Eq. (25), we can define the mean supersaturation loss rate per droplet as $R_w = L_w/n_w(t)$ and reformulate this critical droplet number concentration as $n_w^{(2)}(t) = \frac{P_w}{R_w}$. As time evolves and S_v increases, so too will the number concentration of droplets, $n_w^{(1)}(t)$. At some threshold time, the number concentration of droplets will be equal to the critical droplet number concentration; i.e. $n_w^{(1)}(t) = n_w^{(2)}(t)$. Assuming the plume saturation ratio has equilibrated, no further activation can take place after this time (Twomey, 1959). Hence, this condition defines a lower bound for the maximum number of water droplets that can form during the mixing process, providing an estimate for the contrail ice crystal number concentration. This process forms the basis of the K15 model approach, for which several extensions are described in Sect. 3.3.

3.2 Model extensions for K15

The original K15 model only considers aircraft-emitted nvPM and ambient particles, both of which contain a single particle type and are described using assumed lognormal particle size distribution characteristics and κ. This approach is applicable to nvPM particles because their size distribution characteristics do not change significantly over time and because κ is dominated by the insoluble nvPM fraction. This approach is also applicable to ambient solution droplets because, once entrained into the plume, these droplets are readily activated due to the high ($S_v \gg 1$) plume supersaturations. Therefore, small changes in their size distribution characteristics that are not captured by the K15 model are relatively insignificant. Considering this, our first extension to the K15 model is to introduce plume vPM (Yu et al., 1998) as an additional particle type. We define plume vPM to consist of condensable gaseous material, including (but not limited to) sulfuric acid, organic material, and engine lubrication oil. Simulations show that the size distribution characteristics of plume vPM evolve over time due to condensational growth and coagulation (Kärcher et al., 2000). However, here we are concerned with the contrail formation phase 0.1–1 s into plume dilution, so we prescribe plume vPM properties expected at these timescales. As such, our model cannot be used to *predict* the properties of plume vPM. Instead, we *prescribe* plume vPM using a fixed emission index, κ, and particle size distribution characteristics, and we evaluate the model sensitivity to these variables under typical ranges. In Sect. S5, we also investigate the use of a more complex ambient particle description comprising seven independent particle types. The particle size distribution characteristics and hygroscopicity of these particle types are estimated using outputs from the global aerosol–climate model ECHAM-HAM (Zhang et al., 2012). Overall, we suggest that incorporating these additional ambient particle types could enhance AEI_{ice} by 1 order of magnitude when most ice crystals form via ambient particles. Next, there are several microphysical processes within the K15 model which are described using analytical approximations. Our extensions focus on either improving the accuracy of these approximations or removing them altogether in favour of numerical solutions. Firstly, the analytical approximation used to estimate the activated number concentrations for a given particle type can lead to overpredictions for $S_v < S_{v,c}(d_g, \kappa, T)$ (Sect. S6). To address this, we updated the methodology to estimate activated particle number concentrations using an exact analytical solution.

Secondly, the K15 model estimates $S_{v,c}(T, d_d, \kappa)$ using an approximate analytical solution derived from Eq. (9). We compared this with the full numerical solution and show that the K15 approximation systematically underpredicts critical supersaturations for κ (< 0.2), with larger discrepancies upon reducing d_g (Sect. S7). Hence, we solve Eq. (9) numerically when identifying critical supersaturations, in line with Bier and Burkhardt (2022).

The aforementioned approximations each indirectly relate to the P_w term; however, the final approximation relates to the L_w term. The methodology for estimating contrail ice crystal number concentrations outlined in K15 relies on analytical solutions for both P_w and L_w. In Sect. S8, we provide an overview of the relevant equations used to estimate L_w and give an account of the various approximations used in its derivation. After considering these, we suggest the following modification. The solution to L_w provided in K15 is valid only for when particle activation occurs more quickly than droplet growth, i.e. the "slow-growth" regime (Kärcher and Lohmann, 2002b). After incorporating a plume vPM particle mode, this condition is not necessarily satisfied, so we use a regime-independent analytical solution (Kärcher et al., 2006).

There are two outstanding limitations in the extended K15 model that cannot be resolved. Firstly, we found no means of introducing the Kelvin correction into the solution for L_w (via the droplet growth equation). Omitting the Kelvin effect in the droplet growth equation acts to increase the radial growth rate (Sect. S2). Hence, the ability for droplets to deplete the plume supersaturation is increased, so a lower droplet number concentration is required to quench the ambient supersaturation. This effect is relevant for smaller particles such as plume vPM, where the magnitude of the Kelvin correction is increased. Secondly, an analytical solution for

the inner integral of Eq. (25) requires that L_w is independent of the plume supersaturation so that droplet formation at time $t_0 < t$ does not deplete the plume supersaturation at time t. However, as defined in Eq. (25), L_w is coupled to the plume supersaturation via the droplet growth equation. We anticipate this may be problematic when two or more particle types with comparable number concentrations but different $S_{v,c}$ coexist. Here, one particle type will preferentially activate and grow, subsequently depleting the supersaturation available for the second particle type and thereby inhibiting its activation and growth. For this reason, the extended K15 does not account for the temporal depletion of supersaturation or competition between particle types.

3.3 Model modifications for pyrcel

pyrcel is a 0D cloud parcel model used to simulate the evolution of a parcel of air as it ascends adiabatically at a constant updraft speed (Rothenberg and Wang, 2016). The model is initialised by defining the aerosol population using lognormal particle size distributions, which are discretised into bins. These particle properties are used in combination with the initial ambient conditions to establish an equilibrium wet-particle size distribution. Next, the conservation relations Eqs. (11), (13), and (21) are iterated forward in time, and the wet-particle radii within each bin are tracked using a Lagrangian grid. For a fuller description of the underlying model mechanics, the reader is directed to the original paper and references therein (Rothenberg and Wang, 2016). In contrast to the K15 model, pyrcel explicitly considers the feedback of water vapour between different droplet populations and P_w. However, pyrcel was originally written to describe the formation of warm-phase clouds; therefore, several modifications were made for application to contrail formation.

Firstly, we replace the original P_w term (deriving from parcel updraft) with the definition in Eq. (18). Secondly, we remove the time dependence of altitude and pressure, under the assumption of an adiabatic expansion at constant atmospheric pressure as described in Sect. 3.1. Finally, we derive initial particle number concentrations for the aircraft modes from the associated emission indices using Eqs. (18) and (19). After these changes, the modified pyrcel model and extended K15 models provide an identical description of P_w. However, the coupling of P_w to L_w is fully represented only within the modified pyrcel model.

Additionally, we also extended pyrcel to include homogeneous ice nucleation within growing water droplets. For a complete description of the relations used to arrive at an estimate for the homogeneous ice nucleation temperature, the reader is directed to Sect. S1. In brief, we estimate the rate of homogeneous ice nucleation within a droplet using its water activity (Koop et al., 2000), identified using Eq. (8) as in Lewellen (2020). The probability for ice nucleation within the droplet is then determined by assuming a pulse-like freezing process according to the methodology employed in K15. If the probability equals unity, we assume that the supercooled droplet freezes. The growth of ice crystals by deposition of (ice) supersaturated water vapour is then described using equations analogous to those in Sect. S2, where water saturation in the numerator is replaced with ice saturation, which represents the driving force for vapour deposition. For additional information on the exact form of these expressions, the reader is directed towards Pruppacher and Klett (2010). As outlined above, our implementation is sufficiently flexible to capture homogeneous ice nucleation events within droplets that may not (yet) be considered activated ($d_w < d_{w,c}$).

3.4 Assumed particle properties

We use a conservative parameter space for the properties of each particle mode; see Table 1. We note that both EI_{nvPM} and the particle size distribution characteristics can change with the use of sustainable aviation fuel (SAF) (Märkl et al., 2024; Schripp et al., 2022); however, these fall within larger uncertainties in our simulations. Recently, contrail parcel model simulations have been performed assuming a smaller $d_{g,nvPM}$, consistent with the primary particle diameter rather than the aggregate particle diameter (Yu et al., 2024). While the ice-nucleating ability of larger soot particles has been shown to depend on particle morphology (Marcolli et al., 2021), there is a paucity of data available for activation and ice nucleation on surrogate aircraft nvPM. Therefore, here we choose to identify $d_{g,nvPM}$ as the aggregate particle diameter in line with other studies (Kärcher et al., 2015). Nevertheless, we evaluate the model sensitivity to the choice of nvPM primary particle or aggregate diameter in detail (see Sect. S10) and find that (i) AEI_{ice} predictions agree within 40 % and that (ii) the functional behaviour is similar. Finally, we assume that the nvPM mode contains a 1 wt % coating of soluble material as observed for ground-based emissions testing at moderate fuel sulfur content (FSC) (Gysel et al., 2003) and is therefore characterised by $\kappa = 0.005$ in accordance with the original K15.

The properties of the ambient mode are taken directly from the original K15 model inputs. We argue that these properties are sufficient to investigate the competition between the three modes under most conditions; however, a more sophisticated description would be required to examine sensitivity if most ice crystals formed via ambient particles (Bier et al., 2024); see Sect. S5.

For the plume vPM mode, we identify a provisional size range of $1 < d_{g,vPM} / \mathrm{nm} < 4$ and a $\sigma_{g,vPM}$ of 1.3 (Kärcher et al., 2000; Yu et al., 1998). Similarly, we assume a fixed emission index $EI_{vPM} = 10^{17}\,\mathrm{kg}^{-1}$ in line with modelling and observational evidence (Arnold et al., 2000; Haverkamp et al., 2004; Schumann et al., 2002; Sorokin and Mirabel, 2001). This is also supported by newer observational evidence (Voigt et al., 2025) that the total particle emission index (particle sizes > 5 nm) is on the order $10^{15}\,\mathrm{kg}^{-1}$, which

is consistent with $EI_{vPM} = 10^{17}\,kg^{-1}$ if $d_{g,vPM} = 2.7\,nm$ and $d_{g,vPM} = 1.3$. Concerning particle hygroscopicity, we assume a mixed plume vPM mode comprising sulfuric acid ($\kappa = 0.5$) and condensable POM, for which we use a conservative lower bound of $\kappa = 0$ in line with measurements of non-hygroscopic lubrication oil droplets (Ponsonby et al., 2024). However, we acknowledge that the value of κ for condensable POM is likely to vary with changes in fuel and/or engine architecture. To that end, we evaluate our sensitivity analyses in the extreme cases of both sulfur-rich plume vPM (volume mixing ratio of 95 : 5 sulfuric acid : condensable POM; $0.05 \cdot \kappa_{POM} + 0.95 \cdot \kappa_{H2SO4} \sim 0.5$) and organic-rich plume vPM (volume mixing ratio of 5 : 95 for sulfuric acid : condensable POM; $0.95 \cdot \kappa_{POM} + 0.05 \cdot \kappa_{H2SO4} \sim 0.01$). In Sect. S9, we investigate the impact of assuming all plume vPM particles have the same chemical composition (κ). To achieve this, we divide the plume vPM mode into two distinct plume vPM modes, prescribing these with identical physical characteristics but dissimilar κ. We find that the results of the two-mode system are similar to those of the single-mode system, with a modified value of κ. Therefore, we argue that our range of κ is sufficient to capture a degree of variation in chemical composition *between* vPM particles.

In the above, we have described vPM characteristics at the timescale of particle activation and droplet growth in the nascent contrail mixing plume ($\sim 1\,s$). Separately, we can also estimate the (maximum) equilibrium plume vPM diameters ($d_{eq,vPM}$) that would be reached at $t \gg 1\,s$ using a mass balance. Among other factors, the characteristics of the plume vPM particle size distribution are constrained by the quantity of available sulfuric acid and POM. The former contribution is produced by oxidation of FSC,

$$EI_{H_2SO_4} = \frac{98}{32}\varepsilon_s FSC, \tag{26}$$

where ε_s is the conversion efficiency of sulfur to sulfuric acid, which is typically on the order of 3 % (Yu et al., 2024). The latter contribution represents the sum of condensable gaseous emissions, which has previously been estimated in the range 1–40 $mg\,kg^{-1}$ for relevant, combustion-related organics (Yu et al., 1999) in addition to potential non-combustion lubrication oil emissions of $110\,mg\,kg^{-1}$ (Decker et al., 2024). As outlined in Sect. 1, we can assume that the plume vPM mode can be treated as monomodal, as the smaller mode (i) requires a higher critical supersaturation for activation and (ii) is effectively scavenged by the larger mode. Conservation of mass enables us to estimate $d_{eq,vPM}$ for the plume vPM mode (Kärcher et al., 2000):

$$\frac{\pi}{6} d_{eq,vPM}^3 \rho_{vPM} EI_{vPM} = \frac{98}{32}\varepsilon_s FSC + EI_{POM}, \tag{27}$$

where ρ_{vPM} is the density of the volatile mode. Using Eq. (27), we can therefore estimate $d_{eq,vPM}$ for given EI_{POM} and FSC, which is explored in Sect. 4.5.

4 Results

Here, we present the results of both the extended K15 model and the modified pyrcel models. Based on these results, we then use the modified pyrcel models to run a set of sensitivity analyses and explore how the apparent emission index of ice crystals (AEI_{ice}) within a contrail depends upon particle properties (Sect. 4.3 and 4.5), T_A (Sect. 4.4), and aircraft parameters (Sect. 4.6).

4.1 Contrail mixing behaviour

Figure 4 shows the typical mixing behaviour as predicted by extended K15 and modified pyrcel models. These are compared to profiles in the absence of any particle intervention (SAC-type mixing behaviour), which is encapsulated by P_w. In both the extended K15 model and the modified pyrcel model, the partial pressure of water within the plume follows a similar trend. When the conditions in the plume are subsaturated (i.e. $S_v < 1$), both models align with SAC-type mixing behaviour, since very few particles can activate. Hence, $L_w \sim 0$, and the mixing is dominated by P_w. However, once the plume becomes supersaturated, a proportion of the particles activate to form aqueous solution/water droplets. Here, L_w gradually increases to a maximum, before equilibrating with P_w at water-saturated conditions.

This process of "activation–relaxation" (see warmer-temperature vertical regions of the blue lines in Fig. 4) is approximated within the extended K15 model by estimating the supersaturation at which this takes place and an associated timescale; see Sect. S8. Note that, because particles require supersaturated conditions to activate ($S_{v,c} > 1$), the onset temperature for "activation–relaxation" within the extended K15 model occurs after the point of intersection between the contrail mixing line and p_{liq}. These findings are in qualitative agreement with the modified pyrcel outputs, although they cannot be directly compared. Moreover, the temperature difference is more pronounced for lower EI_{nvPM} ($\sim 2,5\,K$ for $EI_{nvPM} = 10^{15}\,kg^{-1}, 10^{12}\,kg^{-1}$), as the number-weighted particle diameter is smaller, which increases $S_{v,c}$. This again highlights the importance of considering particle properties when determining the point at which most particles activate (see Sect. 2.3).

4.2 Peak plume supersaturation

On average across EI_{nvPM}, the maximum plume supersaturations predicted by the extended K15 model are $\sim 10\,\%$–$70\,\%$ lower than those predicted by the modified pyrcel model; see Fig. 5. Without plume vPM, the largest discrepancies occur when competition between nvPM and ambient particles is largest (at $EI_{nvPM} \sim 10^{12}\,kg^{-1}$; see Fig. 5a). However, when vPM is included, model discrepancies are largest when most contrail ice crystals form via nvPM; see Fig. 5b. Given that both pyrcel and the extended K15 model employ an iden-

Table 1. Assumed characteristics and associated ranges for each particle type used within our parcel model simulations. List of references in the table: [1] Arnold et al. (2000); [2] Haverkamp et al. (2004); [3] Schumann et al. (2002); [4] Sorokin and Mirabel (2001); [5] Kärcher et al. (2000); [6] Yu et al. (1998); [7] Ponsonby et al. (2024); [8] EASA (2025); [9] Durdina et al. (2024); [10] Petzold et al. (2005); [11] Kärcher et al. (2015).

Mode properties	EI/kg^{-1}	d_g/nm	σ_g/no units	κ/no units
Plume vPM	10^{17} [1–4]	1–4 [5]	1.3 [6]	0–0.5 [7]
nvPM	10^{12}–10^{16} [8]	35 [9]	2.0 [9]	0.005 [10]
Ambient [11]	600 cm^{-3}	30	2.2	0.5

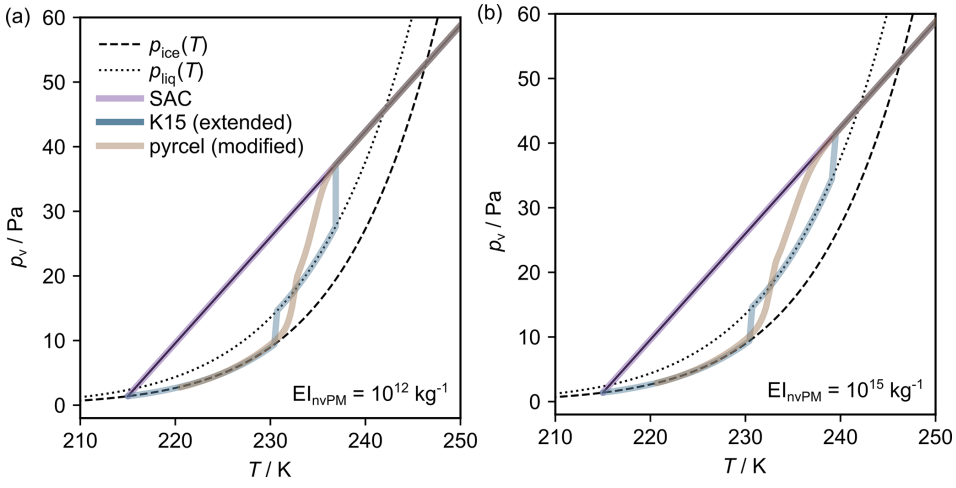

Figure 4. Contrail mixing lines simulated with assumed EI$_{nvPM}$ of **(a)** 10^{12} kg^{-1} and **(b)** 10^{15} kg^{-1}. For both scenarios, the mixing lines are simulated using the original SAC framework (purple lines), the extended K15 model (blue lines), and the modified pyrcel model (brown lines). Each of the simulations has been set to terminate at ice-saturated conditions. These model predictions have been made with plume vPM (EI$_{vPM}$ = 10^{17} kg^{-1}).

tical treatment of P_w (Eq. 18), these model discrepancies must arise from the treatment of L_w. It follows that underestimating the supersaturation at which activation relaxation takes place implies the extended K15 likely overestimates the ability for water droplets to deplete the plume supersaturation. In the final part of Sect. 3.2, we comment on a fundamental limitation of the extended (and original) K15 model that could lead to this discrepancy, which centres around the treatment of L_w. In brief, preparing an analytical solution to Eq. (25) demands that (a) the plume supersaturation is unaffected by particle activation and subsequent droplet growth between adjacent time steps and that (b) the Kelvin effect is discarded from the droplet growth equations. A combination of these effects accounts for the observed behaviour shown in Fig. 5, which underlines the principal limitations of the extended K15 model.

4.3 Sensitivity to EI$_{nvPM}$

In Fig. 6, we show how the ice crystal number concentration scales with EI$_{nvPM}$ in both the extended K15 and modified pyrcel models. This is presented in terms of AEI$_{ice}$, using Eq. (22), so that the results can be more readily compared to other model predictions. Without plume vPM, we find the model agreement for AEI$_{ice}$ is within 35 % when EI$_{nvPM}$ < 10^{16} kg^{-1}; see Fig. 6a. When plume vPM is included, we find that, under this range of EI$_{nvPM}$, differences in model predictions for AEI$_{ice}$ and $s_{v,max}$ exhibit similar trends; see Fig. 5b. Note that AEI$_{ice}$ predictions made using the modified pyrcel model were found to have a maximum uncertainty of ±10 %; see Sect. S11. These derive principally from discretising the vPM mode, which necessarily approximates the analytic particle size distribution; see Sect. S4. These errors are shown in Fig. 6 and in future analysis, where appropriate.

For EI$_{nvPM}$ ≥ 10^{16} kg^{-1}, the extended K15 predicts higher AEI$_{ice}$ than the modified pyrcel model because the extended K15 model does not consider feedback of water vapour between water droplets and ice crystals. To illustrate this effect, suppose we identify a temperature that is warm enough to avoid homogeneous ice nucleation but nonetheless cool enough to promote substantial particle activation, we find that the characteristics of the activated nvPM particles are different in the limit of small and large EI$_{nvPM}$. Note that these limiting values depend on particle size distribution

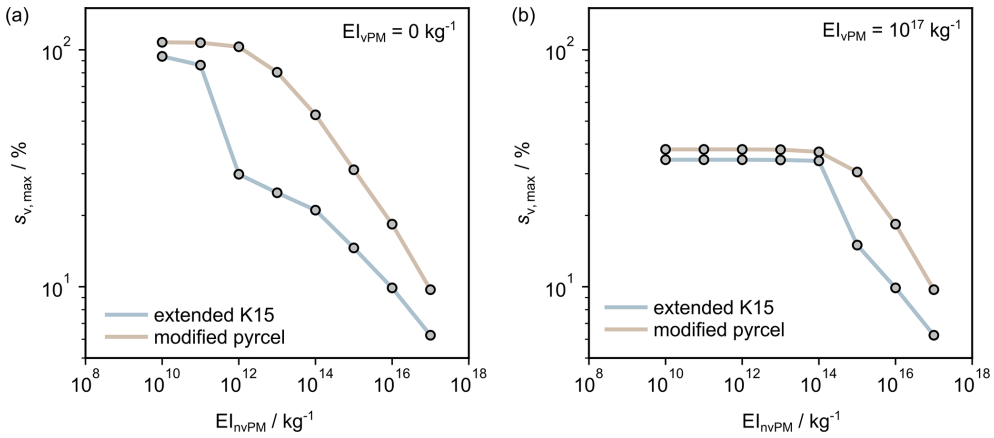

Figure 5. The maximum plume supersaturation ($s_{v,max}$) across a range of EI_{nvPM} as predicted by the modified pyrcel (brown lines) and extended K15 (blue lines) models. These model predictions have been made **(a)** without and **(b)** with the presence of plume vPM ($EI_{vPM} = 10^{17}\,kg^{-1}$).

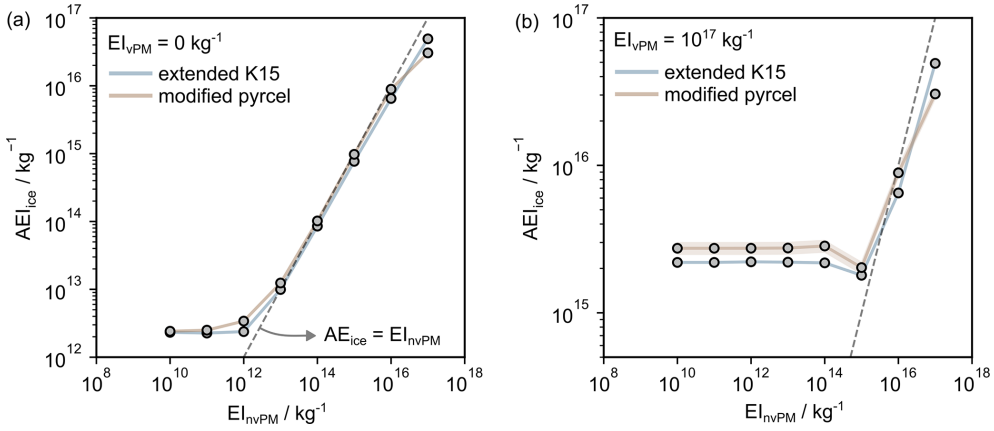

Figure 6. The dependence of contrail AEI_{ice} on EI_{nvPM} as predicted by the modified pyrcel and extended K15 models. Model predictions have been made without **(a)** and with **(b)** the inclusion of plume vPM.

characteristics and properties specified for the contrail mixing line; however, in the case of Fig. 6b, they are separated at $EI_{nvPM} \sim 10^{16}\,kg^{-1}$. To that end, for $EI_{nvPM} \geq 10^{16}\,kg^{-1}$, the available water vapour in the plume is distributed among many particles, and activated nvPM particles typically have values $d_w - d_d < 200$ nm. Comparatively, for $EI_{nvPM} < 10^{16}\,kg^{-1}$, the nvPM wet-particle diameters are distributed quasi-normally and have values $d_w - d_d > 200$ nm. For this reason, the condition for homogeneous ice nucleation is satisfied for each activated nvPM particle for $EI_{nvPM} < 10^{16}\,kg^{-1}$, since this is sensitive to the relative difference between wet- and dry-particle diameters, $d_w - d_d$. Hence, we find that the AEI_{ice} is always at least as large as the apparent emission index of activated particles. By comparison, for $EI_{nvPM} \geq 10^{16}\,kg^{-1}$, given that the smaller activated nvPM particles have comparatively low $d_w - d_d$, their size is more sensitive to changes in local supersaturation. Therefore, when the largest activated nvPM particles begin to nucleate ice, this can result in smaller activated nvPM particles evaporating at their expense. In general terms, this is referred to as the Wegener–Bergeron–Findeisen (WBF) process (Korolev, 2007) and provides a rationale for the opposite trend observed in Figs. 6 and 5 for $EI_{nvPM} \geq 10^{16}\,kg^{-1}$.

We have previously discussed the importance of vapour feedback between growing droplets and the evolving contrail mixing plume as a source of model agreement, highlighting the coupled nature of growing droplets. These effects are exacerbated by the WBF process, which implies that coupled feedback of water vapour occurring between ice crystals and growing droplets can also contribute to model disagreement. Only the modified pyrcel model is able to describe the kinetic treatment of vapour feedback between hydrometeors and the contrail mixing plume. For this reason, we can place more confidence in model predictions made by the modified pyrcel model than the extended K15 model. Additionally, inclusion of the Kelvin effect in the radial growth equation is only rep-

resented in the modified pyrcel model, which is critical for describing water uptake on plume vPM. Hence, we choose to use the modified pyrcel model for the following sensitivity studies.

4.4 Sensitivity to ambient temperature

An evaluation of the modified pyrcel model sensitivity across a range of T_A and EI_{nvPM} revealed several key findings (Fig. 7). Firstly, AEI_{ice} follows a quasi-linear relationship with EI_{nvPM} only when EI_{nvPM} exceeds a temperature-dependent threshold that ranges between 10^{13} and $10^{16}\,kg^{-1}$. In this quasi-linear region, most ice crystals form via nvPM particles, which defines the "soot-rich" regime. Increasing T_A decreases the peak plume supersaturation so that a reduced proportion of the nvPM particles can activate (Bräuer et al., 2021), which has a similar effect to decreasing $d_{g,nvPM}$ (see Sect. S10). The threshold EI_{nvPM} marks the point at which an equal number of contrail ice crystals are formed via nvPM particles and other particles in the plume. Therefore, below this threshold, EI_{nvPM}, the majority of ice crystals do not form via nvPM particles, which defines the "soot-poor" regime. Owing to the results in Fig. 7, "soot-poor" conditions always satisfy the baseline condition $EI_{nvPM} \leq 10^{12}\,kg^{-1}$. Here, for warmer T_A ($\sim T_{SAC}$), most contrail ice crystals form via ambient particles, and AEI_{ice} approaches an asymptotic limit governed by the assumed ambient particle number concentration. Recall that most ambient particles assumed in our simulations (see Table 1) are able to activate at $\Delta T_{SAC} < 1\,K$ (see Fig. 3). As T_A is reduced further ($< T_{SAC}$), the increased peak plume supersaturation enables a greater proportion of plume vPM particles to activate (in addition to the ambient particles), and the limiting value of AEI_{ice} increases. Generally, the position of the threshold EI_{nvPM} increases with decreasing T_A as a larger proportion of vPM particles can activate and therefore compete with nvPM particles for the plume supersaturation (Yu et al., 2024). These findings suggest that the EI_{nvPM} threshold separating the "soot-rich" and "soot-poor" regime should not be treated as a fixed value but rather as a dynamic threshold that varies with T_A.

4.5 Sensitivity to plume vPM properties

Before continuing with our analysis, we emphasise that $d_{eq,vPM}$ calculated using Eq. (27) provide us with an *upper bound* on the diameter of the volatile mode prior to maximum plume supersaturation; due to the kinetics of particle growth, this diameter is likely reached only after a timescale of minutes to hours (Kärcher et al., 2000). Furthermore, it is possible that some volatile material may condense on nvPM (if present), which would further reduce $d_{eq,vPM}$. Therefore, the equilibrium plume vPM diameters quoted in Fig. 8a should only be interpreted as upper bounds.

Figure 8a shows that d_{vPM} increases with EI_{POM} and FSC. For high FSC values ($\sim 1000\,ppm$), $d_{eq,vPM}$ can reach values upwards of 10 nm. By contrast, for low FSC, the size becomes limited by POM, without which $d_{eq,vPM}$ reaches 2–3 nm at most. In Fig. 8b, we use the hygroscopicity parameter for sulfuric acid and POM (assuming $\kappa_{POM} = 0$) to show how the critical saturation ratio depends on both FSC and POM. For low FSC and EI_{POM}, critical supersaturations exceeding 100 % are required for particle activation. However, the presence of nvPM typically precludes such high supersaturations (see Fig. 5); therefore, given that $d_{g,vPM} \leq d_{eq,vPM}$, volatile contributions to AEI_{ice} are likely low in the "soot-rich" regime. On the other hand, with increasing FSC, plume vPM activation becomes increasingly likely, as there are fewer nvPM particles available to quench the plume supersaturation.

As discussed, the results presented above are valid only for providing insight into the approximate equilibrium behaviour of plume vPM formation. Within a real contrail mixing plume, the time available for volatile particle growth by accretion of POM and/or sulfuric acid is reduced, and kinetics become important. To that end, the dependence of volatile mode characteristics on POM (including lubrication oil) and FSC has previously been investigated in simulations performed at cruise (Cantin et al., 2025; Rojo et al., 2015) and ground level (Jones and Miake-Lye, 2024; Wong et al., 2014, 2015). Next, we investigate the dependence of contrail AEI_{ice} on prescribed vPM properties in the modified pyrcel model

Figure 9 demonstrates the sensitivity of the modified pyrcel model to the properties of the plume vPM mode in the "soot-poor" regime, subject to our assumptions on the hygroscopicity of the condensable POM. Our results suggest that a sulfur-rich plume vPM mode can lead to $AEI_{ice} > 10^{15}\,kg^{-1}$, even when $d_{g,vPM} < 2\,nm$. Conversely, when the plume vPM mode is organic-rich, the AEI_{ice} only rises above $10^{15}\,kg^{-1}$ under extremal conditions (i.e. low T_A and high $d_{g,vPM}$). For most other cases, $AEI_{ice} \ll 10^{15}\,kg^{-1}$, and the organic-rich plume vPM mode competes with ambient particles for plume supersaturation. Therefore, if soot particle emissions could be reduced in the vicinity of $10^{12}\,kg^{-1}$, provided the volatile particle mode is largely composed of sulfuric acid, we anticipate only a small reduction in AEI_{ice} values relative to "soot-rich" exhausts. On the other hand, if the volatile particle mode is largely composed of organic material, we find that AEI_{ice} values could be reduced by a factor of up to 100, with benefits ultimately constrained by the size of the plume vPM particles and the properties of entrained ambient particles.

4.6 Sensitivity to aircraft parameters

The final sensitivity analysis will focus on the gradient of the SAC contrail mixing line (Kärcher et al., 2015), which contains important information about aircraft and fuel properties; see Sect. 2.1. Simultaneously, we will explore the sensitivity to ambient temperature so that the resulting output,

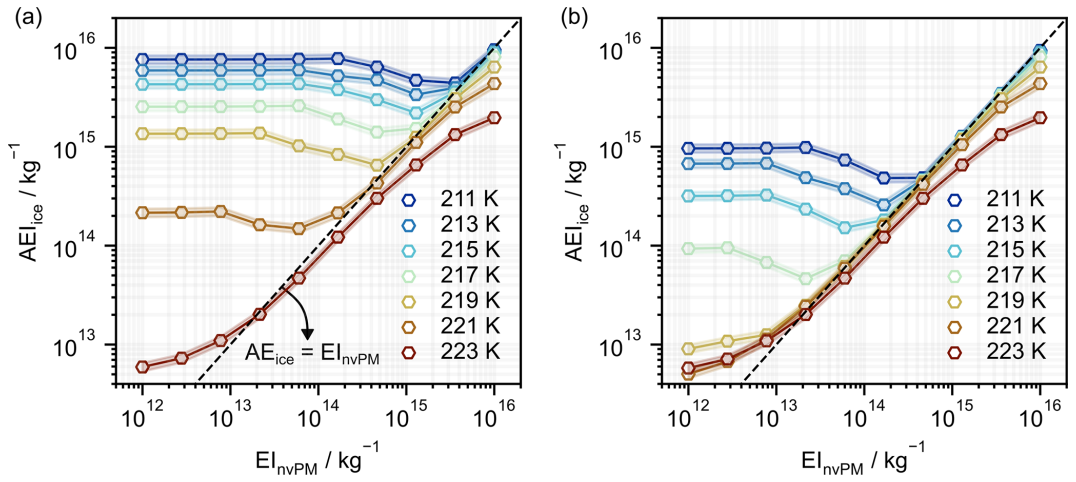

Figure 7. The dependence of contrail AEI_{ice} on T_A (211–223 K, corresponding to ΔT_{SAC} of 2–13 K) and EI_{nvPM} for **(a)** sulfur-rich and **(b)** organic-rich plume vPM.

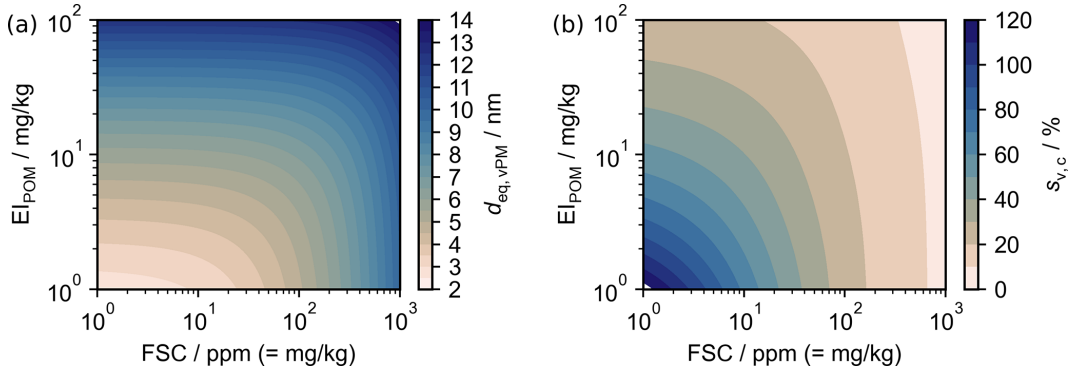

Figure 8. **(a)** Equilibrium volatile particle modal diameter as a function of fuel sulfur content and the emission index of organic particulate matter, assuming a monomodal distribution and omitting the condensation of plume vPM on nvPM. **(b)** Peak plume supersaturation required to activate volatile particles described in panel **(a)**. We have approximated $EI_{vPM} = 1 \times 10^{17}$, $\varepsilon = 3\,\%$, and ρ_{vPM} as a mass-weighted sum of the densities of sulfuric acid and POM (1800 and 1000 kg m^{-3}, respectively), assuming ideal mixing.

AEI_{ice} (G, T_A), provides a useful reference for estimating AEI_{ice} for various combinations of aircraft properties and ambient conditions under "soot-poor" conditions, as defined in Sect. 4.4. For both these scenarios, a sulfur-rich volatile mode was prescribed, as in Sect. 3.4.

Figure 10 shows how the AEI_{ice} varies as a function of G and T_A for "soot-poor" baseline conditions as described in Sect. 4.4 and sulfur-rich plume vPM. For a fixed ambient temperature, increasing G leads to an increased peak plume supersaturation and hence an increase in AEI_{ice}. For ambient temperatures with $\Delta T_{SAC} > 10$ K (here, $T_A > 215$ K), enhancements of up to 3 orders of magnitude are observed within the prospective range of G values for kerosene-based fuel (1.1–2.2). This aligns with results from the original SAC framework, namely that parameters such as overall efficiency (Schumann, 2000), cruise altitude (Gryspeerdt et al., 2024), and water vapour emissions are critical for estimating the resulting contrail ice crystal properties and hence the radiative impact of contrail cirrus.

5 Implications

Here, we contextualise several of the key findings from Sect. 4 for global contrail simulations (Sect. 5.1), contrail mitigation (Sect. 5.2), and engine and fuel technologies (Sect. 5.3).

5.1 Global contrail simulations

Several contrail simulations rely on nvPM (and ambient particle) properties to parameterise AEI_{ice} in young contrails (Bier and Burkhardt, 2022; Teoh et al., 2024). In the "soot-poor" regime, we find that including the activation of plume vPM might enhance AEI_{ice} by up to 3 orders of magnitude. Increased AEI_{ice} is correlated with contrail RF (Burkhardt

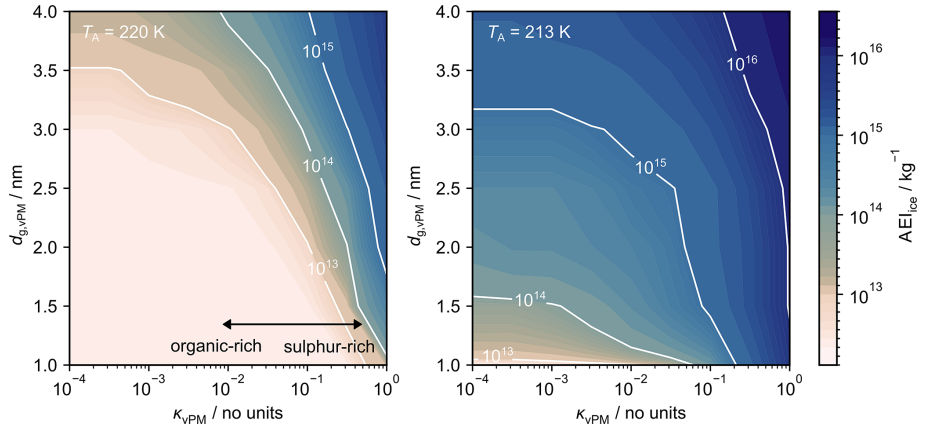

Figure 9. The dependence of contrail AEI_{ice} on the plume vPM properties ($d_{g,vPM}$ and κ_{vPM}) at ambient temperatures of **(a)** 220 K and **(b)** 213 K. For both scenarios, the assumed particle properties are outlined in Table 1; EI_{vPM} and EI_{nvPM} are assumed to be 10^{17} and 10^{12} kg^{-1}, respectively (in line with the "soot-poor" baseline conditions described in Sect. 4.4); and the contrail AEI_{ice} is simulated using the modified pyrcel model with model time steps of 0.1 ms and a maximum duration of 0.5 s.

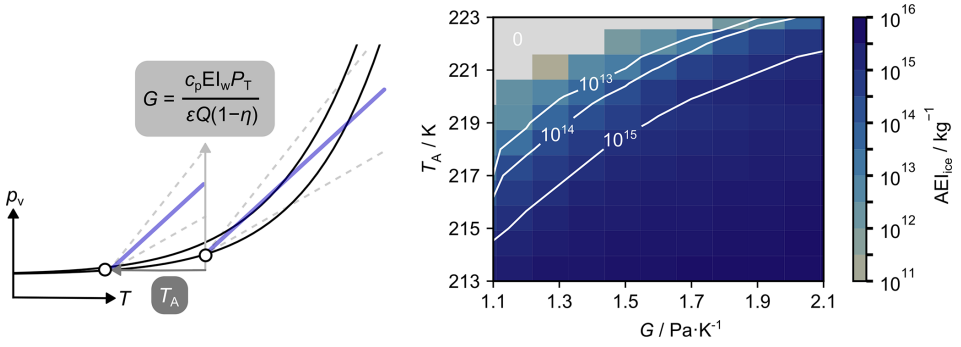

Figure 10. The dependence of contrail AEI_{ice} on T_A and the gradient of the contrail mixing line, as defined in Eq. (1). The simulation was performed for sulfur-rich plume vPM and EI_{nvPM} of 10^{12} kg^{-1}, in line with the "soot-poor" baseline conditions described in Sect. 4.4. The region shaded in grey corresponds to $AEI_{ice} = 0$. Physically, this represents mixing lines that do not intersect the water saturation line.

et al., 2018), implying that these current global contrail simulations may underestimate global contrail forcing. Importantly, as the AEI_{ice} predictions are sensitive to the assumed properties of plume vPM and as these are highly uncertain at present, a global contrail simulation relying on the extended K15 model would serve only as a sensitivity study.

5.2 Contrail mitigation

Operational contrail mitigation has hitherto focused on circumventing regions where $s_i > 0$ in order to mitigate contrail *persistence*. Our simulations imply that, under "soot-poor" conditions and for flights within 5 K of T_{SAC}, increasing the ambient temperature by 2 K may reduce AEI_{ice} by up to a factor of 10 (see Fig. 9). If this behaviour could be experimentally validated, an analogous strategy might be possible by circumventing cooler regions of the upper troposphere, to mitigate contrail *formation* under "soot-poor" conditions. Moreover, maximum predictive biases between the European Centre for Medium-Range Weather Forecasts (ECMWF) ERA5 atmospheric reanalysis model and In-service Aircraft for A Global Observing System (IAGOS) observations of T_A and s_i are −0.2 % and −5.5 %, respectively (Wolf et al., 2025), which implies that atmospheric requirements for contrail *formation* can be predicted more accurately than for contrail *persistence*. Assuming an upper-tropospheric lapse rate of −6.5 K km^{-1} per the ICAO standard atmosphere (ICAO, 1993), a 2 K temperature difference corresponds to approximately 10 flight levels (1000 ft or 305 m). This is equivalent to the reduced vertical separation minima between aircraft in the FL 290–FL 410 flight band (ICAO, 2012), which implies that it might be possible to adjust T_A by making relatively small changes in elevation. Using T_A data from ECMWF, we explore this further in Sect. S12. Nevertheless, avoidance of local cold spots would likely involve reducing aircraft cruise altitudes, which may increase (a) the likelihood for aircraft emissions to perturb clouds in the mixed-phase regime, (b) the number of turbulence events (Dehghan et al., 2014), and (c) direct emissions of CO_2. Therefore, we reiterate that

this approach is subject to both inherent model uncertainties and the aforementioned concerns (a)–(c), which need to be resolved before this is explored further.

5.3 Engine and fuel technologies

Aircraft powered by lean-burn combustors have EI_{nvPM} that range between 10^{10} and $10^{12}\,kg^{-1}$ (EASA, 2025), which coincides with our definition for the "soot-poor" regime given in Sect. 4.4. Under these conditions, AEI_{ice} is controlled by the properties of plume vPM emissions and T_A (see Fig. 9). Therefore, AEI_{ice} can be reduced practically by (a) avoiding cooler ambient temperatures (see Sect. 5.1) and (b) reducing the mass of condensable volatile material. To that end, we suggest the removal of lubrication oil emissions and diminution of FSC. In Sect. 4.4, we demonstrate that FSC scales with the mass of condensable sulfuric acid. Therefore, for fixed EI_{vPM}, increasing FSC may produce plume vPM particles with higher $d_{g,vPM}$ and higher κ_{vPM}. This intuition agrees with results collated across various flight campaigns, showing that EI_{vPM} for particles larger than 5 nm increases with increasing FSC (Schumann et al., 2002). In the "soot-poor" regime, AEI_{ice} and hence the potential contrail climate impact increase with $d_{g,vPM}$ and κ_{vPM}. Therefore, we would advise that FSC is reduced as low as practicably possible, as FSC levels of several ppm (assuming $EI_{POM} = 0\,kg^{-1}$) are sufficient to produce plume vPM particles with $d_{eq,vPM}$ on the order of several nm (see Sect. 4.5). We note that comparable FSC reductions have been successfully demonstrated in other sectors (IMO, 2022) and that the largest benefits would be achieved if low-FSC fuels were used in lean-burn engines, where AEI_{ice} values are most sensitive to the properties of plume vPM emissions.

Finally, measurements show that SAF can reduce both EI_{nvPM} and $d_{g,nvPM}$ relative to conventional fuel (Moore et al., 2017; Voigt et al., 2021). Under conditions where most contrail ice crystals form via nvPM particles, both changes would reduce AEI_{ice}, as fewer particles are able to activate at a given supersaturation. These effects have previously been reported using contrail parcel model simulations to compare with ECLIF (Emission and CLimate Impact of alternative Fuels) measurements (Yu et al., 2024). Additionally, for variable EI_{nvPM} and fixed plume vPM properties, decreasing $d_{g,nvPM}$ would increase the position of the minimum in Fig. 9 (see Sect. S10).

6 Conclusions

Here, we extended two parcel models to describe particle microphysics during the early stages ($t < 1$ s) of contrail plume evolution. Firstly, the minimal framework originally developed by Kärcher et al. (2015) was extended to account for plume vPM by incorporating an additional particle mode. We replaced several analytical approximations with numerical solutions and increased the accuracy of others so that the model could be more applicable for describing the activation of plume vPM. Secondly, using similar parameterisations for the mixing process but a higher-fidelity description of L_w, a cloud parcel model (pyrcel) (Rothenberg and Wang, 2016) was modified to treat contrail formation and used as a benchmark for model comparison.

We found the extended K15 model systematically underpredicted the peak plume supersaturations when compared to the modified pyrcel model. This is likely because it does not incorporate the Kelvin effect and therefore overpredicts droplet growth rates. Generally, the estimated AEI_{ice} from both models are within 35 % for $EI_{nvPM} \leq 10^{16}\,kg^{-1}$, when activation of plume vPM is excluded. However, when plume vPM activation is included, the modified pyrcel model predicts higher ice crystal number concentrations by 10 %–30 % for $EI_{nvPM} \leq 10^{13}\,kg^{-1}$. Discrepancies are more pronounced for $EI_{nvPM} > 10^{13}\,kg^{-1}$ due to differing treatment of kinetics and water vapour competition between hydrometeors between models.

Using the modified pyrcel model, we performed several sensitivity studies and found that, across EI_{nvPM}, the AEI_{ice} decreases with decreasing peak plume supersaturations as predicted by the original SAC mixing line. This is controlled by the ambient relative humidity, T_A, and the gradient of the mixing line. Therefore, decreasing the overall efficiency and water vapour emissions results in fewer contrail ice crystals being produced. Also, we find that the threshold between "soot-rich" and "soot-poor" conditions (as defined in Sect. 4.4) is sensitive to the properties of plume vPM (EI_{vPM}, $d_{g,vPM}$, κ_{vPM}) and T_A and should therefore be treated as a dynamic threshold. Notably, we find that the threshold EI_{nvPM} increases with decreasing T_A as an increasing proportion of vPM particles are able to compete with nvPM particles for the plume supersaturation. In the "soot-poor" regime, including plume vPM activation leads to AEI_{ice} enhancements by up to 3 orders of magnitude; these are maximised if the material is highly hygroscopic (e.g. sulfur-rich).

As the aviation industry reduces EI_{nvPM} and therefore approaches the "soot-poor" regime, we find that existing contrail cirrus models that do not extend to include plume vPM activation will underestimate AEI_{ice} and therefore global climate forcing. Future research should be directed towards (i) ground-based and in situ measurements focusing on the "soot-poor" regime and its transition towards the "soot-rich" regime, with near-field characterisation of *both* nvPM and plume vPM properties; (ii) laboratory measurements of the activation properties and/or ice-nucleating ability of particles representative of plume vPM present in nascent contrail exhausts; and (iii) validation of plume aerosol and contrail formation models (parcel model/LES simulations) using in situ observations.

Appendix A: Notation

SAC	Schmidt–Appleman Criterion
nvPM	Non-volatile particulate matter
vPM	Volatile particulate matter
EI_{vPM}, EI_{nvPM}	Number emission index of vPM, nvPM
SAF	Sustainable aviation fuel
d_g	Geometric mean diameter
σ_g	Geometric standard deviation
K15	Microphysical model developed by Kärcher et al. (2015)
T_E	Gas temperature at the engine exit plane
T_A	Ambient temperature
T	Plume temperature
G	Gradient of average contrail mixing line
$p_{v,M}$	Partial pressure of water vapour in the contrail mixing plume
$p_{v,E}$	Partial pressure of water vapour at the engine exit plane
$p_{v,A}$	Partial pressure of water vapour in the ambient environment
c_p	Isobaric specific heat capacity of air
EI_w	Mass emission index of water vapour
P_T	Total air pressure
ε	Ratio of gas constants for water vapour and dry air
Q	Total heat released per mass of fuel burned
η	Overall aircraft efficiency
p_{liq}, p_{ice}	Saturation vapour pressure above a plane surface of supercooled water, ice
$S_{v,M}$, $S_{i,M}$	Water, ice saturation ratio in a contrail mixing plume
$s_{v,M}$	Water supersaturation in a contrail mixing plume
T_{SAC}	SAC temperature
ΔT_{SAC}	Difference between the ambient and SAC temperatures (T_{SAC}–T_A)
S_v	Water saturation ratio above a liquid droplet
a_w	Water activity
σ_s	Surface tension at the droplet–air interface
M_w	Molar mass of water
ρ_w	Density of water
R	Global gas constant
d_w	Wet-particle diameter
d_d	Dry-particle diameter
κ	Hygroscopicity parameter
$d_{w,c}$, $r_{w,c}$	Critical wet-particle diameter, radius
$S_{v,c}$	Critical water saturation ratio
w_v	Water vapour mixing ratio
w_c	Mixing ratio of condensed water vapour
P_w	Water (super)saturation production rate in the absence of particles
L_w	Water (super)saturation depletion rate due to particle activation and droplet growth
β	Plume dilution parameter
D	Plume dilution factor
τ_m	Timescale over which contrail mixing is unaffected by entrainment
N_0	Mass-based mixing factor
n_T	Total number concentration of aircraft-mode particles
$n_{a,T}$	Total number concentration of ambient-mode particles
$n_{a,0}$	Ambient particle number concentration
ρ_a	Mass density of ambient air
$\dot{r}_w$	Radial droplet growth rate
n_w	Droplet number concentration
$\dot{n}_w$	Rate of change of droplet number concentration
FSC	Fuel sulfur content
POM	Particulate organic matter
$EI_{H_2SO_4}$	Mass emission index of sulfuric acid
EI_{POM}	Mass emission index of POM
ε_s	Conversion efficiency of sulfur to sulfuric acid
$d_{eq,vPM}$	vPM equilibrium diameter
ρ_{vPM}	Density of condensed vPM
θ_G	threshold contrail formation temperature at p_{liq}

Code and data availability. Code for the modified pyrcel model and extended K15 model is available at https://doi.org/10.5281/zenodo.16901327 (Rothenberg et al., 2025) and https://doi.org/10.5281/zenodo.16901290 (Ponsonby, 2025). The results shown in study can be generated using this code.

Supplement. The supplement related to this article is available online at https://doi.org/10.5194/acp-25-18617-2025-supplement.

Author contributions. JP and MEJS conceptualised the project. JP developed the software, conducted the initial investigation, and wrote the original article. All the authors developed the methodology and edited the article. MEJS supervised the project and acquired funding.

Competing interests. The contact author has declared that none of the authors has any competing interests.

Disclaimer. Publisher's note: Copernicus Publications remains neutral with regard to jurisdictional claims made in the text, published maps, institutional affiliations, or any other geographical representation in this paper. While Copernicus Publications makes every effort to include appropriate place names, the final responsibility lies with the authors. Views expressed in the text are those of the authors and do not necessarily reflect the views of the publisher.

Acknowledgements. We would like to thank Daniel Rothenberg for helpful discussions on revising pyrcel to describe contrail formation, Fangqun Yu for his insight on the model description of plume vPM, and Christiane Voigt for useful discussions on model comparison with in situ measurement data. Finally, we would like to thank Yu Wang for providing the ECHAM-HAM data used in Sect. S5.

Financial support. This research has been supported by the Engineering and Physical Sciences Research Council (grant no. EP/S023593/1). Funding was also received from the European Union's Horizon Europe Research and Innovation programme (grant agreement no. 101192301).

Review statement. This paper was edited by Ken Carslaw and reviewed by two anonymous referees.

References

Airbus: Airbus Global Market Forecast 2025–2044, https://www.airbus.com/en/products-services/commercial-aircraft/global-market-forecast/ (last access: 14 October 2025), 2024.

Arnold, F., Kiendler, A., Wiedemer, V., Aberle, S., Stilp, T., and Busen, R.: Chemiion concentration measurements in jet engine exhaust at the ground: Implications for ion chemistry and aerosol formation in the wake of a jet aircraft, Geophysical Research Letters, 27, 1723–1726, https://doi.org/10.1029/1999GL011096, 2000.

Bier, A. and Burkhardt, U.: Impact of Parametrizing Microphysical Processes in the Jet and Vortex Phase on Contrail Cirrus Properties and Radiative Forcing, JGR Atmospheres, 127, e2022JD036677, https://doi.org/10.1029/2022JD036677, 2022.

Bier, A., Unterstrasser, S., and Vancassel, X.: Box model trajectory studies of contrail formation using a particle-based cloud microphysics scheme, Atmos. Chem. Phys., 22, 823–845, https://doi.org/10.5194/acp-22-823-2022, 2022.

Bier, A., Unterstrasser, S., Zink, J., Hillenbrand, D., Jurkat-Witschas, T., and Lottermoser, A.: Contrail formation on ambient aerosol particles for aircraft with hydrogen combustion: a box model trajectory study, Atmos. Chem. Phys., 24, 2319–2344, https://doi.org/10.5194/acp-24-2319-2024, 2024.

Bräuer, T., Voigt, C., Sauer, D., Kaufmann, S., Hahn, V., Scheibe, M., Schlager, H., Diskin, G. S., Nowak, J. B., DiGangi, J. P., Huber, F., Moore, R. H., and Anderson, B. E.: Airborne Measurements of Contrail Ice Properties – Dependence on Temperature and Humidity, Geophysical Research Letters, 48, e2020GL092166, https://doi.org/10.1029/2020GL092166, 2021.

Burkhardt, U., Bock, L., and Bier, A.: Mitigating the contrail cirrus climate impact by reducing aircraft soot number emissions, npj Clim Atmos Sci, 1, 37, https://doi.org/10.1038/s41612-018-0046-4, 2018.

Cantin, S., Chouak, M., and Garnier, F.: Effects of fuel sulfur content and nvPM emissions on contrail formation: A CFD-microphysics study including the role of organic compounds, Journal of Aerosol Science, 188, 106612, https://doi.org/10.2139/ssrn.5138455, 2025.

Cumpsty, N. A.: Jet propulsion: a simple guide to the aerodynamics and thermodynamic design and performance of jet engines, 2nd ed., Cambridge University Press, Cambridge, U.K., New York, NY, USA, 303 pp., 2003.

Decker, Z. C. J., Alpert, P. A., Ammann, M., Anet, J. G., Bauer, M., Cui, T., Durdina, L., Edebeli, J., Gysel-Beer, M., Prévôt, A. S. H., Qi, L., Slowik, J. G., Spirig, C., Tinorua, S., Ungeheuer, F., Vogel, A., Zhang, J., and Brem, B. T.: Emission and Formation of Aircraft Engine Oil Ultrafine Particles, ACS EST Air, 1, 1662–1672, https://doi.org/10.1021/acsestair.4c00184, 2024.

Dehghan, A., Hocking, W. K., and Srinivasan, R.: Comparisons between multiple in situ aircraft turbulence measurements and radar in the troposphere, Journal of Atmospheric and Solar-Terrestrial Physics, 118, 64–77, https://doi.org/10.1016/j.jastp.2013.10.009, 2014.

Durdina, L., Durand, E., Edebeli, J., Spirig, C., Brem, B. T., Elser, M., Siegerist, F., Johnson, M., Sevcenco, Y. A., and Crayford, A. P.: Characterizing and Predicting nvPM Size Distributions for Aviation Emission Inventories and Environmental Impact, Environ. Sci. Technol., 58, 10548–10557, https://doi.org/10.1021/acs.est.4c02538, 2024.

EASA: ICAO Aircraft Engine Emissions Databank, https://www.easa.europa.eu/en/domains/environment/icao-aircraft-engine-emissions-databank (last access date: 14 October 2025), 2025.

Ferreira, T., Alonso, J. J., and Gorlé, C.: Developing a Numerical Framework for the High-Fidelity Simulation of Contrails: Sensitivity Analysis for Conventional Contrails, in: AIAA AVIATION FORUM AND ASCEND 2024, AIAA AVIATION FORUM AND ASCEND 2024, Las Vegas, Nevada, https://doi.org/10.2514/6.2024-3775, 2024.

Grewe, V., Gangoli Rao, A., Grönstedt, T., Xisto, C., Linke, F., Melkert, J., Middel, J., Ohlenforst, B., Blakey, S., Christie, S., Matthes, S., and Dahlmann, K.: Evaluating the climate impact of aviation emission scenarios towards the Paris agreement including COVID-19 effects, Nat Commun, 12, 3841, https://doi.org/10.1038/s41467-021-24091-y, 2021.

Gryspeerdt, E., Stettler, M. E. J., Teoh, R., Burkhardt, U., Delovski, T., Driver, O. G. A., and Painemal, D.: Operational differences lead to longer lifetimes of satellite detectable contrails from more fuel efficient aircraft, Environ. Res. Lett., 19, 084059, https://doi.org/10.1088/1748-9326/ad5b78, 2024.

Gysel, M., Nyeki, S., Weingartner, E., Baltensperger, U., Giebl, H., Hitzenberger, R., Petzold, A., and Wilson, C. W.: Properties of jet engine combustion particles during the PartEmis experiment: Hygroscopicity at subsaturated conditions, Geophysical Research Letters, 30, 2003GL016896, https://doi.org/10.1029/2003GL016896, 2003.

Haverkamp, H., Wilhelm, S., Sorokin, A., and Arnold, F.: Positive and negative ion measurements in jet aircraft engine exhaust: concentrations, sizes and implications for aerosol formation, Atmospheric Environment, 38, 2879–2884, https://doi.org/10.1016/j.atmosenv.2004.02.028, 2004.

ICAO: Manual Of The Icao Standard Atmosphere – extended to 80 kilometres / 262,500 feet (Doc 7488), 3rd edn., https://store.icao.int/en/manual-of-the-icao-standard-atmosphere-extended-to-80-kilometres-262500-feet-doc-7488 (last access 14 October 2025), 1993.

ICAO: Manual on Implementation Vertical Separation (Doc 9574), 3rd edn., https://store.icao.int/en/manual-on-implementation-vertical-separation-doc-9574 (last access 14 October 2025), 2012.

IMO: Amendment MEPC.234(75) of the International Convention for the Prevention of Pollution from Ships (MARPOL) Annex VI: Regulations for the Prevention of Air Pollution from Ships, https://wwwcdn.imo.org/localresources/en/OurWork/

Environment/Documents/Airpollution/MEPC.324(75).pdf (last access: 14 October 2025), 2022.

Jones, S. H. and Miake-Lye, R. C.: Parameterization of H_2SO_4 and organic contributions to volatile PM in aircraft plumes at ground idle, Journal of the Air & Waste Management Association, 74, 490–510, https://doi.org/10.1080/10962247.2024.2354820, 2024.

Kärcher, B.: Formation and radiative forcing of contrail cirrus, Nat Commun, 9, 1824, https://doi.org/10.1038/s41467-018-04068-0, 2018.

Kärcher, B. and Fahey, D. W.: The role of sulfur emission in volatile particle formation in jet aircraft exhaust plumes, Geophysical Research Letters, 24, 389–392, https://doi.org/10.1029/97GL00119, 1997.

Kärcher, B. and Lohmann, U.: A Parameterization of cirrus cloud formation: Homogeneous freezing including effects of aerosol size, Journal of Geophysical Research: Atmospheres, 107, AAC 9-1–AAC 9-10, https://doi.org/10.1029/2001JD001429, 2002a.

Kärcher, B. and Lohmann, U.: A parameterization of cirrus cloud formation: Homogeneous freezing of supercooled aerosols, Journal of Geophysical Research: Atmospheres, 107, AAC 4-1–AAC 4-10, https://doi.org/10.1029/2001JD000470, 2002b.

Kärcher, B. and Yu, F.: Role of aircraft soot emissions in contrail formation, Geophysical Research Letters, 36, 2008GL036649, https://doi.org/10.1029/2008GL036649, 2009.

Kärcher, B., Turco, R. P., Yu, F., Danilin, M. Y., Weisenstein, D. K., Miake-Lye, R. C., and Busen, R.: A unified model for ultrafine aircraft particle emissions, J. Geophys. Res., 105, 29379–29386, https://doi.org/10.1029/2000JD900531, 2000.

Kärcher, B., Hendricks, J., and Lohmann, U.: Physically based parameterization of cirrus cloud formation for use in global atmospheric models, Journal of Geophysical Research: Atmospheres, 111, https://doi.org/10.1029/2005JD006219, 2006.

Kärcher, B., Burkhardt, U., Bier, A., Bock, L., and Ford, I. J.: The microphysical pathway to contrail formation, JGR Atmospheres, 120, 7893–7927, https://doi.org/10.1002/2015JD023491, 2015.

Kärcher, B., Marcolli, C., and Mahrt, F.: The Role of Mineral Dust Aerosol Particles in Aviation Soot-Cirrus Interactions, JGR Atmospheres, 128, e2022JD037881, https://doi.org/10.1029/2022JD037881, 2023.

Khou, J. C., Ghedhaïfi, W., Vancassel, X., Montreuil, E., and Garnier, F.: CFD simulation of contrail formation in the near field of a commercial aircraft: Effect of fuel sulfur content, metz, 26, 585–596, https://doi.org/10.1127/metz/2016/0761, 2017.

Khou, J.-C., Ghedhaïfi, W., Vancassel, X., and Garnier, F.: Spatial Simulation of Contrail Formation in Near-Field of Commercial Aircraft, Journal of Aircraft, 52, 1927–1938, https://doi.org/10.2514/1.C033101, 2015.

Koop, T., Luo, B., Tsias, A., and Peter, T.: Water activity as the determinant for homogeneous ice nucleation in aqueous solutions, Nature, 406, 611–614, https://doi.org/10.1038/35020537, 2000.

Korolev, A.: Limitations of the Wegener–Bergeron–Findeisen Mechanism in the Evolution of Mixed-Phase Clouds, Journal of the Atmospheric Sciences, 64, 3372–3375, https://doi.org/10.1175/JAS4035.1, 2007.

Korolev, A. V. and Mazin, I. P.: Supersaturation of Water Vapor in Clouds, Journal of the Atmospheric Sciences, 60, 2957–2974, https://doi.org/10.1175/1520-0469(2003)060<2957:SOWVIC>2.0.CO;2, 2003.

Kumar, P., Sokolik, I. N., and Nenes, A.: Parameterization of cloud droplet formation for global and regional models: including adsorption activation from insoluble CCN, Atmos. Chem. Phys., 9, 2517—2532, https://doi.org/10.5194/acp-9-2517-2009, 2009.

Lee, D. S., Fahey, D. W., Skowron, A., Allen, M. R., Burkhardt, U., Chen, Q., Doherty, S. J., Freeman, S., Forster, P. M., Fuglestvedt, J., Gettelman, A., De León, R. R., Lim, L. L., Lund, M. T., Millar, R. J., Owen, B., Penner, J. E., Pitari, G., Prather, M. J., Sausen, R., and Wilcox, L. J.: The contribution of global aviation to anthropogenic climate forcing for 2000 to 2018, Atmospheric Environment, 244, 117834, https://doi.org/10.1016/j.atmosenv.2020.117834, 2021.

Lewellen, D. C.: A Large-Eddy Simulation Study of Contrail Ice Number Formation, Journal of the Atmospheric Sciences, 77, 2585–2604, https://doi.org/10.1175/JAS-D-19-0322.1, 2020.

Lewellen, D. C., Meza, O., and Huebsch, W. W.: Persistent Contrails and Contrail Cirrus. Part I: Large-Eddy Simulations from Inception to Demise, Journal of the Atmospheric Sciences, 71, 4399–4419, https://doi.org/10.1175/JAS-D-13-0316.1, 2014.

Marcolli, C., Mahrt, F., and Kärcher, B.: Soot PCF: pore condensation and freezing framework for soot aggregates, Atmos. Chem. Phys., 21, 7791–7843, https://doi.org/10.5194/acp-21-7791-2021, 2021.

Märkl, R. S., Voigt, C., Sauer, D., Dischl, R. K., Kaufmann, S., Harlaß, T., Hahn, V., Roiger, A., Weiß-Rehm, C., Burkhardt, U., Schumann, U., Marsing, A., Scheibe, M., Dörnbrack, A., Renard, C., Gauthier, M., Swann, P., Madden, P., Luff, D., Sallinen, R., Schripp, T., and Le Clercq, P.: Powering aircraft with 100 % sustainable aviation fuel reduces ice crystals in contrails, Atmos. Chem. Phys., 24, 3813–3837, https://doi.org/10.5194/acp-24-3813-2024, 2024.

Moore, R. H., Thornhill, K. L., Weinzierl, B., Sauer, D., D'Ascoli, E., Kim, J., Lichtenstern, M., Scheibe, M., Beaton, B., Beyersdorf, A. J., Barrick, J., Bulzan, D., Corr, C. A., Crosbie, E., Jurkat, T., Martin, R., Riddick, D., Shook, M., Slover, G., Voigt, C., White, R., Winstead, E., Yasky, R., Ziemba, L. D., Brown, A., Schlager, H., and Anderson, B. E.: Biofuel blending reduces particle emissions from aircraft engines at cruise conditions, Nature, 543, 411–415, https://doi.org/10.1038/nature21420, 2017.

Murphy, D. M. and Koop, T.: Review of the vapour pressures of ice and supercooled water for atmospheric applications, Q. J. R. Meteorol. Soc., 131, 1539–1565, https://doi.org/10.1256/qj.04.94, 2005.

Murray, B. J., O'Sullivan, D., Atkinson, J. D., and Webb, M. E.: Ice nucleation by particles immersed in supercooled cloud droplets, Chem. Soc. Rev., 41, 6519, https://doi.org/10.1039/c2cs35200a, 2012.

Paoli, R., Nybelen, L., Picot, J., and Cariolle, D.: Effects of jet/vortex interaction on contrail formation in supersaturated conditions, Physics of Fluids, 25, 053305, https://doi.org/10.1063/1.4807063, 2013.

Petters, M. D. and Kreidenweis, S. M.: A single parameter representation of hygroscopic growth and cloud condensation nucleus activity, Atmos. Chem. Phys., 7, 1961–1971, https://doi.org/10.5194/acp-7-1961-2007, 2007.

Petzold, A., Fiebig, M., Fritzsche, L., Stein, C., Schumann, U., Wilson, C. W., Hurley, C. D., Arnold, F., Katragkou, E., Baltensperger, U., Gysel, M., Nyeki, S., Hitzenberger, R., Giebl, H., and Hughes, K.: Particle emissions from aircraft engines a

survey of the European project PartEmis, metz, 14, 465–476, https://doi.org/10.1127/0941-2948/2005/0054, 2005.

Picot, J., Paoli, R., Thouron, O., and Cariolle, D.: Large-eddy simulation of contrail evolution in the vortex phase and its interaction with atmospheric turbulence, Atmos. Chem. Phys., 15, 7369–7389, https://doi.org/10.5194/acp-15-7369-2015, 2015.

Ponsonby, J.: jponvc/extended-K15-model: extended K15 model (v1.0), Zenodo [code], https://doi.org/10.5281/zenodo.16901290, 2025.

Ponsonby, J., King, L., Murray, B. J., and Stettler, M. E. J.: Jet aircraft lubrication oil droplets as contrail ice-forming particles, Atmos. Chem. Phys., 24, 2045–2058, https://doi.org/10.5194/acp-24-2045-2024, 2024.

Pruppacher, H. R. and Klett, J. D.: Microphysics of clouds and precipitation, in: Atmospheric and Oceanographic Sciences Library, 2nd edn., Springer Dordrecht, 714 pp., ISBN: 9780792342113, 2010.

Rogers, R. R. and Yau, M. K.: A short course in cloud physics, in: International Series in Natural Philosophy, 3rd edn., Butterworth-Heinemann, Burlington, Massachusetts, Vol. 113, ISBN: 9780750632157, 1996.

Rojo, C., Vancassel, X., Mirabel, P., Ponche, J.-L., and Garnier, F.: Impact of alternative jet fuels on aircraft-induced aerosols, Fuel, 144, 335–341, https://doi.org/10.1016/j.fuel.2014.12.021, 2015.

Rothenberg, D. and Wang, C.: Metamodeling of Droplet Activation for Global Climate Models, Journal of the Atmospheric Sciences, 73, 1255–1272, https://doi.org/10.1175/JAS-D-15-0223.1, 2016.

Rothenberg, D., Ponsonby, J., and lompar: jponvc/pyrcel-for-contrails: pyrcel for contrails (v1.0), Zenodo [code], https://doi.org/10.5281/zenodo.16901327, 2025.

Saffaripour, M., Thomson, K. A., Smallwood, G. J., and Lobo, P.: A review on the morphological properties of non-volatile particulate matter emissions from aircraft turbine engines, Journal of Aerosol Science, 139, 105467, https://doi.org/10.1016/j.jaerosci.2019.105467, 2020.

Schripp, T., Anderson, B. E., Bauder, U., Rauch, B., Corbin, J. C., Smallwood, G. J., Lobo, P., Crosbie, E. C., Shook, M. A., Miake-Lye, R. C., Yu, Z., Freedman, A., Whitefield, P. D., Robinson, C. E., Achterberg, S. L., Köhler, M., Oßwald, P., Grein, T., Sauer, D., Voigt, C., Schlager, H., and LeClercq, P.: Aircraft engine particulate matter emissions from sustainable aviation fuels: Results from ground-based measurements during the NASA/DLR campaign ECLIF2/ND-MAX, Fuel, 325, 124764, https://doi.org/10.1016/j.fuel.2022.124764, 2022.

Schumann, U.: On conditions for contrail formation from aircraft exhausts, Meteorologische Zeitschrift, 4–23, https://doi.org/10.1127/metz/5/1996/4, 1996.

Schumann, U.: Influence of propulsion efficiency on contrail formation, Aerospace Science and Technology, 4, 391–401, https://doi.org/10.1016/S1270-9638(00)01062-2, 2000.

Schumann, U., Arnold, F., Busen, R., Curtius, J., Kärcher, B., Kiendler, A., Petzold, A., Schlager, H., Schröder, F., and Wohlfrom, K.-H.: Influence of fuel sulfur on the composition of aircraft exhaust plumes: The experiments SULFUR 1–7, Journal of Geophysical Research: Atmospheres, 107, AAC 2-1–AAC 2-27, https://doi.org/10.1029/2001JD000813, 2002.

Schumann, U., Mayer, B., Graf, K., and Mannstein, H.: A Parametric Radiative Forcing Model for Contrail Cirrus, J. Appl. Meteorol. Climatol., 51, 1391–1406, https://doi.org/10.1175/JAMC-D-11-0242.1, 2012.

Schumann, U., Baumann, R., Baumgardner, D., Bedka, S. T., Duda, D. P., Freudenthaler, V., Gayet, J.-F., Heymsfield, A. J., Minnis, P., Quante, M., Raschke, E., Schlager, H., Vázquez-Navarro, M., Voigt, C., and Wang, Z.: Properties of individual contrails: a compilation of observations and some comparisons, Atmos. Chem. Phys., 17, 403–438, https://doi.org/10.5194/acp-17-403-2017, 2017.

Seinfeld, J. H. and Pandis, S. N.: Atmospheric chemistry and physics: from air pollution to climate change, 3rd edn., John Wiley & Sons, Inc, New York, 1326 pp., ISBN: 9781118947401, 2016.

Sorjamaa, R. and Laaksonen, A.: The effect of H_2O adsorption on cloud drop activation of insoluble particles: a theoretical framework, Atmos. Chem. Phys., 7, 6175–6180, https://doi.org/10.5194/acp-7-6175-2007, 2007.

Sorokin, A. and Mirabel, P.: Ion recombination in aircraft exhaust plumes, Geophysical Research Letters, 28, 955–958, https://doi.org/10.1029/2000GL011801, 2001.

Sullivan, R. C., Moore, M. J. K., Petters, M. D., Kreidenweis, S. M., Roberts, G. C., and Prather, K. A.: Effect of chemical mixing state on the hygroscopicity and cloud nucleation properties of calcium mineral dust particles, Atmos. Chem. Phys., 9, 3303–3316, https://doi.org/10.5194/acp-9-3303-2009, 2009.

Teoh, R., Schumann, U., Gryspeerdt, E., Shapiro, M., Molloy, J., Koudis, G., Voigt, C., and Stettler, M. E. J.: Aviation contrail climate effects in the North Atlantic from 2016 to 2021, Atmos. Chem. Phys., 22, 10919–10935, https://doi.org/10.5194/acp-22-10919-2022, 2022.

Teoh, R., Engberg, Z., Schumann, U., Voigt, C., Shapiro, M., Rohs, S., and Stettler, M. E. J.: Global aviation contrail climate effects from 2019 to 2021, Atmos. Chem. Phys., 24, 6071–6093, https://doi.org/10.5194/acp-24-6071-2024, 2024.

Testa, B., Durdina, L., Alpert, P. A., Mahrt, F., Dreimol, C. H., Edebeli, J., Spirig, C., Decker, Z. C. J., Anet, J., and Kanji, Z. A.: Soot aerosols from commercial aviation engines are poor ice-nucleating particles at cirrus cloud temperatures, Atmos. Chem. Phys., 24, 4537–4567, https://doi.org/10.5194/acp-24-4537-2024, 2024.

Twomey, S.: The nuclei of natural cloud formation part II: The supersaturation in natural clouds and the variation of cloud droplet concentration, Geofisica Pura e Applicata, 43, 243–249, https://doi.org/10.1007/BF01993560, 1959.

Ungeheuer, F., Caudillo, L., Ditas, F., Simon, M., Van Pinxteren, D., Kýlýç, D., Rose, D., Jacobi, S., Kürten, A., Curtius, J., and Vogel, A. L.: Nucleation of jet engine oil vapours is a large source of aviation-related ultrafine particles, Commun Earth Environ, 3, 319, https://doi.org/10.1038/s43247-022-00653-w, 2022.

Voigt, C., Kleine, J., Sauer, D., Moore, R. H., Bräuer, T., Le Clercq, P., Kaufmann, S., Scheibe, M., Jurkat-Witschas, T., Aigner, M., Bauder, U., Boose, Y., Borrmann, S., Crosbie, E., Diskin, G. S., DiGangi, J., Hahn, V., Heckl, C., Huber, F., Nowak, J. B., Rapp, M., Rauch, B., Robinson, C., Schripp, T., Shook, M., Winstead, E., Ziemba, L., Schlager, H., and Anderson, B. E.: Cleaner burning aviation fuels can reduce contrail cloudiness, Commun Earth Environ, 2, 114, https://doi.org/10.1038/s43247-021-00174-y, 2021.

Voigt, C., Märkl, R., Sauer, D., Dischl, R., Kaufmann, S., Bräuer, T., Jurkat, T., Renard, C., Seeliger, K., Chenadec, G. L., Moreau, J., Yu, F., Bonne, N., Roche, A., Zelina, J., Dörnbrack, A., Eirenschmalz, L., Heckl, C., Horst, E., Lichtenstern, M., Marsing, A., Roiger, A., Scheibe, M., Stock, P., Giez, A., Eckel, G., Neumann, G., Vals, M., Requena-Esteban, E., and Clercq, P. L.: Substantial aircraft contrail formation at low soot emission levels, Nature Portfolio [preprint], https://doi.org/10.21203/rs.3.rs-6559440/v1, 9 May 2025.

Wolf, K., Bellouin, N., Boucher, O., Rohs, S., and Li, Y.: Correction of ERA5 temperature and relative humidity biases by bivariate quantile mapping for contrail formation analysis, Atmos. Chem. Phys., 25, 157–181, https://doi.org/10.5194/acp-25-157-2025, 2025.

Wong, H.-W., Jun, M., Peck, J., Waitz, I. A., and Miake-Lye, R. C.: Detailed Microphysical Modeling of the Formation of Organic and Sulfuric Acid Coatings on Aircraft Emitted Soot Particles in the Near Field, Aerosol Science and Technology, 48, 981–995, https://doi.org/10.1080/02786826.2014.953243, 2014.

Wong, H.-W., Jun, M., Peck, J., Waitz, I. A., and Miake-Lye, R. C.: Roles of Organic Emissions in the Formation of Near Field Aircraft-Emitted Volatile Particulate Matter: A Kinetic Microphysical Modeling Study, Journal of Engineering for Gas Turbines and Power, 137, 072606, https://doi.org/10.1115/1.4029366, 2015.

Yu, F. and Turco, R. P.: The role of ions in the formation and evolution of particles in aircraft plumes, Geophysical Research Letters, 24, 1927–1930, https://doi.org/10.1029/97GL01822, 1997.

Yu, F., Turco, R. P., Kärcher, B., and Schröder, F. P.: On the mechanisms controlling the formation and properties of volatile particles in aircraft wakes, Geophysical Research Letters, 25, 3839–3842, https://doi.org/10.1029/1998GL900012, 1998.

Yu, F., Turco, R. P., and Kärcher, B.: The possible role of organics in the formation and evolution of ultrafine aircraft particles, J. Geophys. Res., 104, 4079–4087, https://doi.org/10.1029/1998JD200062, 1999.

Yu, F., Kärcher, B., and Anderson, B. E.: Revisiting Contrail Ice Formation: Impact of Primary Soot Particle Sizes and Contribution of Volatile Particles, Environ. Sci. Technol., 58, 17650–17660, https://doi.org/10.1021/acs.est.4c04340, 2024.

Zhang, K., O'Donnell, D., Kazil, J., Stier, P., Kinne, S., Lohmann, U., Ferrachat, S., Croft, B., Quaas, J., Wan, H., Rast, S., and Feichter, J.: The global aerosol-climate model ECHAM-HAM, version 2: sensitivity to improvements in process representations, Atmos. Chem. Phys., 12, 8911–8949, https://doi.org/10.5194/acp-12-8911-2012, 2012.

Supplement of Atmos. Chem. Phys., 25, 18617–18637, 2025
https://doi.org/10.5194/acp-25-18617-2025-supplement

Atmospheric Chemistry and Physics
Open Access
EGU

Supplement of

An updated microphysical model for particle activation in contrails: the role of volatile plume particles

Joel Ponsonby et al.

Correspondence to: Marc E. J. Stettler (m.stettler@imperial.ac.uk)

Contents

S1 Homogeneous ice nucleation and κ-Köhler theory

To estimate the homogeneous ice nucleation temperature for supercooled aqueous solution droplets, we employ a similar approach to the original K15 model. This method provides an estimate for the homogeneous temperature of pure water droplets i.e., those forming from wholly insoluble particles $\kappa = 0$. Here, we extend this analysis to include particles that are not wholly insoluble ($\kappa \neq 0$), where the activity of the surrounding solution depends implicitly on the ambient conditions through the wet particle diameter, $d_w = d_w(S_v, T)$ and explicitly on the particle properties, d_d and κ, as described in Sect. 2.2 of the main text. Regardless, homogeneous ice nucleation is governed by the central expression

$$j = J \cdot V_w, \tag{S1}$$

where j is the freezing rate (ice nucleation events per second), which is given as a product of the freezing rate coefficient J (ice nucleation events per unit volume per unit time) and the liquid water volume, $V_w = \frac{4}{3}\pi(r^3 - r_d^3)$. Assuming that a droplet entirely freezes when an ice nucleation event occurs within its volume, j is constrained as the number of droplets freezing per unit time. Previous studies have demonstrated that for typical cloud droplets with diameters of ~μm and homogeneous ice nucleation temperatures of ~235 K, ln(J) scales inversely proportional to temperature (Murray et al., 2010). If we consider a number of identical droplets within a cooling contrail, while plume temperatures are above the common homogeneous ice nucleation temperature ($T > T_{hom}$), although V_w is maximised, j is limited by small J. As the contrail cools and transitions towards T_{hom}, high plume cooling rates (< -10 K/s) lead to a sharp increase in J, maximising j. During the ice nucleation event, V_w is quickly depleted, and j returns to 0. Incidentally, if the droplet size distribution is monomodal, it is typically narrow enough to conform to the same narrative. Based on this semi-quantitative analysis, it is appropriate to assume a pulse-like nature of j and characterise the freezing event by defining a characteristic freezing timescale,

$$\tau_{frz}^{-1} = \frac{\partial \ln(j)}{\partial t} \approx \frac{\partial \ln(J)}{\partial T}\frac{dT}{dt}, \tag{S2}$$

where we have assumed that changes in ln(V_w) are much slower than changes in ln(J). Using Eq. (S2), we can transform Eq. (S1) to estimate the frozen droplet fraction λ (Murray et al., 2012).

$$\lambda = 1 - e^{-J\tau_{frz}V_w}. \tag{S3}$$

For the below analysis, we choose $\lambda = 1 - \delta$ ($\delta = 10^{-20} \sim 0$) in line with previous studies (Kärcher et al., 2015; Lewellen, 2020) and evaluate τ_{frz}^{-1} according to Eq. (S2). We use the freezing rate coefficient described by Koop et al. (2000), which depends *inter alia* on the activity of the solution, $J = J(a_w)$. For a given particle type defined by d_d and κ and at a given temperature, T, first we evaluate d_w and S_v for saturation ratios $S_v < S_{v,c}$. Next, we evaluate $J = J(S_v, T)$ according to the relations outlined in Koop et al. (2000) using an internal droplet pressure (P) parameterization (Marcolli, 2020). This enables us to evaluate $P = P(S_v, T)$ for saturation ratios $S_v < S_{v,c}$. We can then finally determine the critical saturation

ratio, $S_{v,hom}$ at which we satisfy our predefined threshold, $\lambda \sim 1$. This critical saturation ratio represents approximate conditions for homogeneous ice nucleation within the given particle mode.

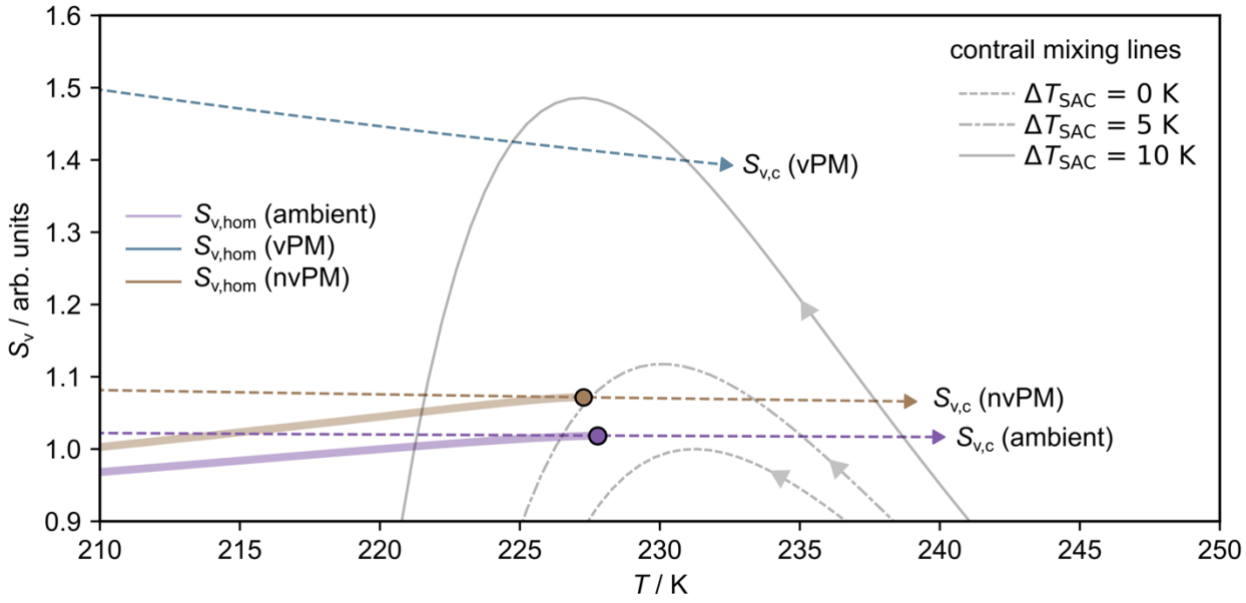

Figure S1: illustrative ice nucleation temperature as predicted using *J* parametrizations from Koop et al. (2000) using the methodology outlined in Kärcher et al. (2015). Particle properties have been taken from Table. 1 in the main text, assuming a sulphur-rich (κ = 0.5) vPM mode with $d_{g,vPM}$ = 4 nm. Several contrail mixing lines have also been presented with G = 1.64.

In Fig. S1, we show the critical saturation ratios required from particle activation and homogeneous ice nucleation, $S_{v,c}$ and $S_{v,hom}$ respectively, for the three particle modes outlined in Table. 1 of the main text for a sulphur-rich vPM mode. The paths traced by $S_{v,hom} = S_{v,hom}(T)$ are also commonly known as "Koop line" freezing thresholds as described by Koop et al. (2000) and in other literature (Baumgartner et al., 2022). For a given particle type, if the ambient conditions lie in the region above the relevant Koop line, the solution droplets are able to freeze homogeneously. The Koop line termini are indicated using coloured markers on Fig. S1, these identify the temperatures beyond which the condition on λ is no longer achieved; for temperatures below the termini, $S_{v,hom}$ asymptotically approaches $S_{v,c}$.We have also shown three contrail mixing lines at three different ambient temperatures corresponding to ΔT_{SAC} of 0 K, 5 K and 10 K. Fig. S1 enables us to determine, for a given particle type, whether particle activation or homogeneous ice nucleation is likely to occur first during the contrail mixing process. We find that for the nvPM and vPM modes (brown and blue lines, respectively), every feasible contrail mixing line first surpasses the critical saturation ratio for droplet activation (bisects $S_{v,c}$) before entering the region above the relevant Koop line. For that reason, we conclude that for the majority of vPM and nvPM particles, droplet activation takes place *prior* to homogeneous ice nucleation. The same conclusion is met for the hygroscopic ambient mode, however for small $\Delta T_{SAC} \sim 0.1$ K, it is possible that a small fraction of the larger particles may freeze homogeneously before they are considered activated. In conclusion, we find that for the three types of particles investigated within this work, we are justified in assuming that particle activation occurs prior to homogeneous ice nucleation.

S2 Radial growth equation

The growth or evaporation of droplets by diffusion of water vapour is described by the radial growth law which may be expressed in the general form (Seinfeld and Pandis, 2016)

$$\frac{dr}{dt} = \frac{G}{r}(S_{\mathrm{e}} - S_{\mathrm{v}}) \,, \tag{S4}$$

where S_{e} is the ambient (environmental) saturation ratio, S_{v} is the equilibrium water saturation ratio above the particle (see Sect. 2.2 of the main text) and G is a growth coefficient. The growth coefficient may be expressed as the sum of two terms, the first of which is associated with heat conduction and the second is associated with water vapour diffusivity (Rogers and Yau, 1996)

$$G = \frac{1}{F_{\mathrm{k}}+F_{\mathrm{d}}};\; F_{\mathrm{k}} = \frac{l_{\mathrm{w}}\rho_{\mathrm{w}}}{4k'_{\mathrm{a}}T}\left(\frac{l_{\mathrm{w}}M_{\mathrm{w}}}{RT} - 1\right),\; F_{\mathrm{d}} = \frac{\rho_{\mathrm{w}}RT}{4e_S^0 D'_{\mathrm{w}}M_{\mathrm{w}}}, \tag{S5}$$

where l_{w} is the latent heat of evaporation of water. Parameters D'_{w} and k'_{a} represent the modified diffusivity (D_{w}) and thermal conductivity (k_{a}), respectively, accounting for non-continuum effects as (Pruppacher and Klett, 2010)

$$k'_{\mathrm{a}} = k_{\mathrm{a}}\Big/\left[1 + \frac{k_a}{\alpha_{\mathrm{T}} r \rho_{\mathrm{w}} c_p}\sqrt{\frac{2\pi M_{\mathrm{a}}}{RT}}\right];\; k_{\mathrm{a}} = 10^{-3}(4.39 + 0.071T), \tag{S6}$$

$$D'_{\mathrm{w}} = D_{\mathrm{w}}\Big/\left[1 + \frac{D_{\mathrm{w}}}{\alpha_{\mathrm{C}} r}\sqrt{\frac{2\pi M_{\mathrm{a}}}{RT}}\right];\; D_{\mathrm{w}} = 2.11 \times 10^{-5}\left(\frac{T}{273.15}\right)^{1.94}\left(\frac{P_0}{P_{\mathrm{T}}}\right), \tag{S7}$$

where we have introduced the heat capacity c_{p} and the thermal accommodation and condensation coefficients, α_{C} and α_{T} respectively (P_0 = 101325 Pa). And, for the purposes of this work, we assume fixed coefficients $\alpha_{\mathrm{T}} = \alpha_{\mathrm{C}} = 1$. If the effects of diffusivity are much greater than thermal conductivity (i.e., $F_{\mathrm{d}} >> F_{\mathrm{k}}$), we can simplify Eq. (S4) and rearrange it into the equivalent form

$$\frac{dr}{dt} = \frac{A}{b_2 r_{\mathrm{w}} + 1};\; \mathrm{A} = \frac{\upsilon\bar{\nu}n_{\mathrm{w}}^{sat}\alpha_{\mathrm{w}}}{4}(S_{\mathrm{e}} - S_{\mathrm{v}}), b_2 = \frac{\bar{\nu}}{4D_{\mathrm{w}}}, \tag{S8}$$

where $\bar{\nu}$ is the mean molecular thermal speed and υ is the molar volume of water. This definition is employed when solving the L_{w} integral within the K15 approach (Ford, 1998, p.20076; Kärcher et al., 2006; Kärcher and Lohmann, 2003) as the functional dependence on r_{w} makes Eq. (S8) more tractable than Eq. (S4).

S3 Limiting behaviour of κ-Köhler theory

We know that the maximum hygroscopicity parameter is on the order $\kappa \sim 1$. Using this value, Eq. (7) in the main text collapses to

$$S_v = \frac{d_\mathrm{w}^3 - d_\mathrm{d}^3}{d_\mathrm{w}^3} e^{\left(\frac{4\sigma_\mathrm{s} M_\mathrm{w}}{RT\rho_\mathrm{w} d_\mathrm{w}}\right)}. \tag{S9}$$

To identify the critical wet particle diameter, $d_{\mathrm{w,c}}$, we can differentiate Eq. (S9) with respect to d_w and set the result equal to zero.

$$\frac{dS_\mathrm{v}}{dd_\mathrm{w}} = \frac{3e^{\frac{a}{d_\mathrm{w}}}}{d_\mathrm{w}} - \frac{e^{\frac{a}{\mathrm{w}}}(-d_\mathrm{d}^3 + d_\mathrm{w}^3)}{d_\mathrm{w}^5} - \frac{3e^{\frac{a}{\mathrm{w}}}(-d_d^3 + d_\mathrm{w}^3)}{d_\mathrm{w}^4} = 0; \quad a = \frac{4\sigma_s M_\mathrm{w}}{RT\rho_\mathrm{w}}, \tag{S10}$$

$$d_{\mathrm{w,c}} = \frac{2^{1/3} d_\mathrm{d}^3}{\left(d_\mathrm{d}^3 \mathrm{a}^3 + \sqrt{-4d_\mathrm{d}^9 \mathrm{a}^3 + d_\mathrm{d}^6 \mathrm{a}^6}\right)^{\frac{1}{3}}} + \frac{\left(d_\mathrm{d}^3 \mathrm{a}^3 + \sqrt{-4d_\mathrm{d}^9 \mathrm{a}^3 + d_\mathrm{d}^6 \mathrm{a}^6}\right)^{\frac{1}{3}}}{2^{1/3}\mathrm{a}}. \tag{S11}$$

To recover the critical water saturation ratio, we can introduce the result from Eq. (S11) into Eq. (S9), which gives us an analytic expression for $S_{\mathrm{v,c}} = S_{\mathrm{v,c}}(a, d_\mathrm{d}, \kappa = 1)$. We find that this analytical function is monotonic, and the solution asymptotically approaches $S_{\mathrm{v,c}} \to 1$ in the limit $d_\mathrm{p} \to \infty$, in agreement with numerical solution used in this work. Therefore, we have demonstrated that within the κ-Köhler framework, even highly hygroscopic materials ($\kappa \sim 1$) cannot achieve critical water saturation ratios that are equivalent to or fall below unity. Only surfaces with zero curvature (plane surfaces) are capable of condensing water at ambient water saturation ratios of unity; for particles with finite diameters, the equality $S_{\mathrm{v,c}} > 1$, is always satisfied.

S4 Extension to lognormal distributions

In the analysis in Sect. 2 of the main text, we have presented arguments under the assumption that all particles within a contrail mixing plume are identical and therefore share the common properties (d_d, κ), which define their activation behaviour. Although this approach is sufficient to gain an insight into the relevance of particle properties, most of the results presented hereafter in this work rely on – and can only be interpreted by - a more sophisticated description of particle properties. To that end, we define a particle type according to its particle size distribution (PSD) (Seinfeld and Pandis, 2016)

$$\frac{dN}{d\ln d_\mathrm{d}} = \frac{N_\mathrm{t}}{\sqrt{2\pi}\ln\sigma_\mathrm{g}} e^{\left[-\frac{(\ln d_\mathrm{d} - \ln d_\mathrm{g})^2}{2(\ln\sigma_\mathrm{g})^2}\right]}, \tag{S12}$$

where N_t represents the total number of particles, σ_g represents the geometric standard deviation (GSD) of the distribution and d_g represents the geometric mean diameter (GMD). Incidentally, the description used in Sect. 2 of the main text is equivalent to taking Eq. (S12) in the limit $\sigma_\mathrm{g} \to 1$, which represents an infinitely narrow distribution comprising particles with a uniform diameter $d_d = d_\mathrm{g}$. Assuming that a given particle type comprises particles with uniform composition and mixing state, we assert that a particle type may be fully described if the properties of its PSD $(d_\mathrm{g}, \sigma_\mathrm{g}, N_\mathrm{t})$ and its total hygroscopicity parameter are known. A consequence of departing from the simplistic description of an infinitely narrow PSD, is that for a given ambient saturation ratio, it is no longer the case that either all or none of the particles are activated (Boolean-type), but rather that some proportion of the particles will be activated. From Sect. 2 of the main text, we know that the critical saturation ratio for activation may be determined if the particle diameter, total hygroscopicity parameter and ambient temperature are known, $S_\mathrm{v,c} = S_\mathrm{v,c}(T, d_\mathrm{d}, \kappa)$. Similarly, this relationship may be inverted to estimate the critical particle diameter, $d_\mathrm{d,c}$, required for activation for a given ambient saturation ratio, $d_\mathrm{d,c} = d_\mathrm{d,c}(T, S_\mathrm{v}, \kappa)$. Because the relationship is monotonic, we know that for a given ambient saturation ratio S_v, all particles with $d_\mathrm{d} > d_\mathrm{d,c}$ will be able to activate. Therefore, for a particle type defined by a total hygroscopicity parameter κ and PSD properties $(d_\mathrm{g}, \sigma_\mathrm{g}, N_\mathrm{t})$, the number of particles that can activate at a given ambient water saturation ratio, S_v, is given by the truncated integral of Eq. (S12) as

$$N = \int_{d_\mathrm{d,c}(T,S_\mathrm{v},\kappa)}^{\infty} \frac{N_\mathrm{t}}{\sqrt{2\pi}\ln\sigma_\mathrm{g}} e^{\left[-\frac{(\ln d_\mathrm{d} - \ln d_\mathrm{g})^2}{2(\ln\sigma_\mathrm{g})^2}\right]} d\ln d_\mathrm{d}. \tag{S13}$$

After changing variables and performing the integration, we arrive at a modified form of the lognormal cumulative distribution function which uses the error function (erf)

$$N = \frac{N_\mathrm{t}}{2}\left[1 - \mathrm{erf}\left(\frac{(\ln d_\mathrm{d,c}(T,S_\mathrm{v},\kappa) - \ln d_\mathrm{g})^2}{2(\ln\sigma_\mathrm{g})^2}\right)\right]. \tag{S14}$$

S5 K15 model extension: particle modes

To extend the description of the ambient particle mode used in K15, results from the global aerosol-climate model ECHAM-HAM (Zhang et al., 2012) were obtained. This model categorises particles into seven classes according to their size and solubility (Vignati et al., 2004): insoluble coarse mode particles and insoluble/soluble nucleation, accumulation and Aitken mode particles. Each class is described by a GMD and GSD and, as an approximation, soluble and insoluble modes are prescribed conservative hygroscopicity parameters of 0.5 and 0 respectively. For the purposes of this work, ECHAM-HAM data for year 2018 were interpolated at the mean altitude of waypoints that satisfied the SAC (Spire Aviation, 2024).

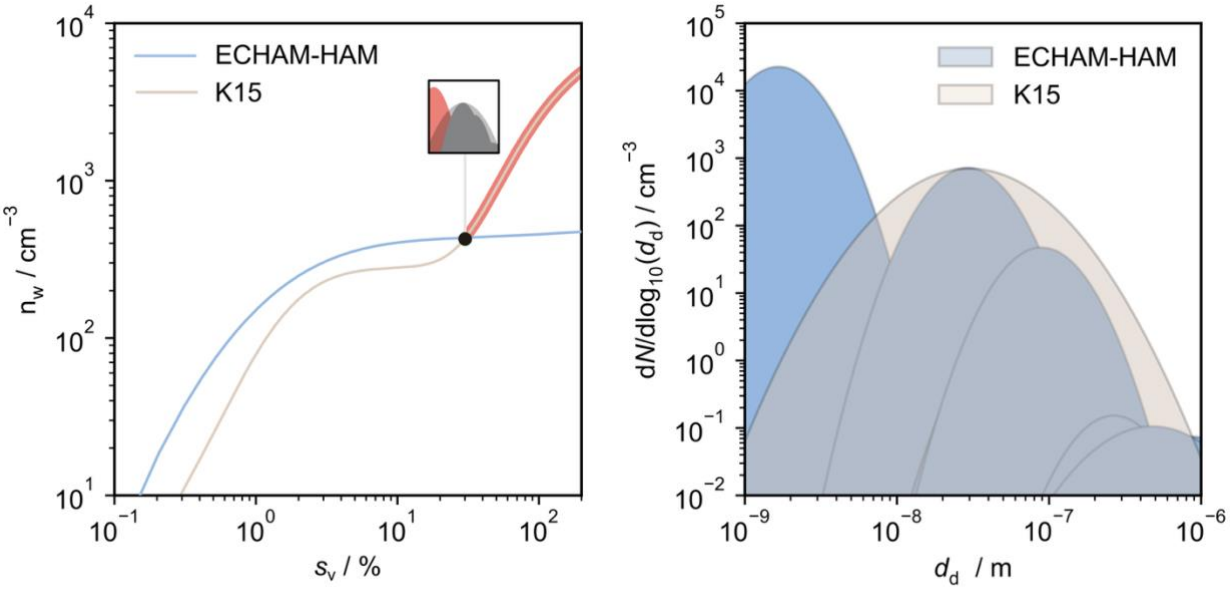

Figure S2: (a) anticipated activated particle number concentration for the original and updated ambient particle modes. Activation of the small, soluble nucleation mode is highlighted, resulting in a pronounced increase in the number concentration of activated particles in the plume (b) comparison of the original and updated ambient particle modes used within the K15 and extended K15 models respectively.

In Fig. S2b, we compare the ambient particle size distribution obtained from the 7-mode ECHAM-HAM model (blue) with the single ambient mode used in the K15 model (beige). The resulting differences in particle activation are shown in Fig. S2a where the total number of activated particles is shown as a function of ambient supersaturation. We find that for moderate supersaturations (s_v < 10 %) both descriptions lead to similar numbers of activated particles. However, if the supersaturation is able to exceed ~ 30 %, the populous soluble nucleation mode is able to activate resulting in a sharp increase in the number of activated particles. Under soot-poor conditions, the absence of a significant condensational sink will typically lead to greater plume supersaturations. Hence, a complete description of the ambient particle mode (including soluble nucleation mode particles) is critical to understanding contrail formation under these conditions (Bier et al., 2022).

S6 K15 model extension: activated fractions

In the K15 model, integration over the PDF to determine activated number concentrations is approximated. The form of the approximation used is given by

$$N \approx \frac{N_t}{1+\left(\frac{d_{\mathrm{d,c}}(T,S_{\mathrm{v}},\kappa)}{d_{\mathrm{g}}}\right)^{\zeta}}, \tag{S15}$$

$$\zeta = \frac{4}{\sqrt{2\pi}} \ln \sigma_{\mathrm{g}}, \tag{S16}$$

where ζ is defined as a size distribution slope parameter.

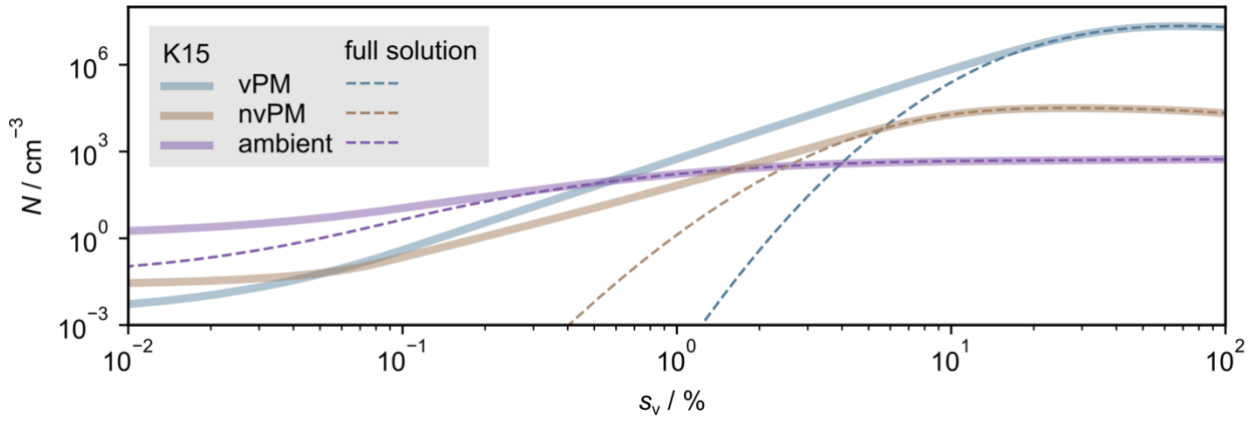

Figure S3: Comparison of the K15 approximation of PDF integration versus full (analytical) solution for the three particle modes as outlined in Table. 1 of the main text.

Fig. S3 shows the agreement between Eq. (S15) and Eq. (S16). Using the particle types outlined in Table. 1 of the main text, we find that for nvPM and ambient particle modes, the K15 approximation is valid for estimates above a supersaturation of ~ 10%. Below this value, the K15 approximation systematically overpredicts activated number concentrations. For the transition and soot-poor regimes, discrepancy between the K15 approximation and the full solution is more prominent, and agreement is only achieved for supersaturations exceeding ~ 20%. For this reason, we choose to use the full solution in our extended K15 model simulations.

S7 K15 model extension: numerical treatment of κ-Köhler theory

In the K15 model, the authors estimate $S_{\mathrm{v,c}}(T, d_{\mathrm{d}}, \kappa)$ using an approximate analytical solution derived from Eq. (7) in the main text, which takes the form

$$\ln S_{\mathrm{v,c}} = \sqrt{\frac{4}{27\kappa}\left(\frac{A}{d_{\mathrm{d}}}\right)^3}\ ;\ A = \frac{4\sigma_{\mathrm{s}} M_{\mathrm{w}}}{RT\rho_{\mathrm{w}}}, \tag{S17}$$

Although analytically tractable, Eq. (S17) is only strictly valid for estimating critical water saturation ratios provided $\kappa >$ 0.2 (Petters and Kreidenweis, 2007). Outside this range, $S_{\mathrm{v,c}}(T, d_{\mathrm{d}}, \kappa)$ must instead be determined by numerical methods.

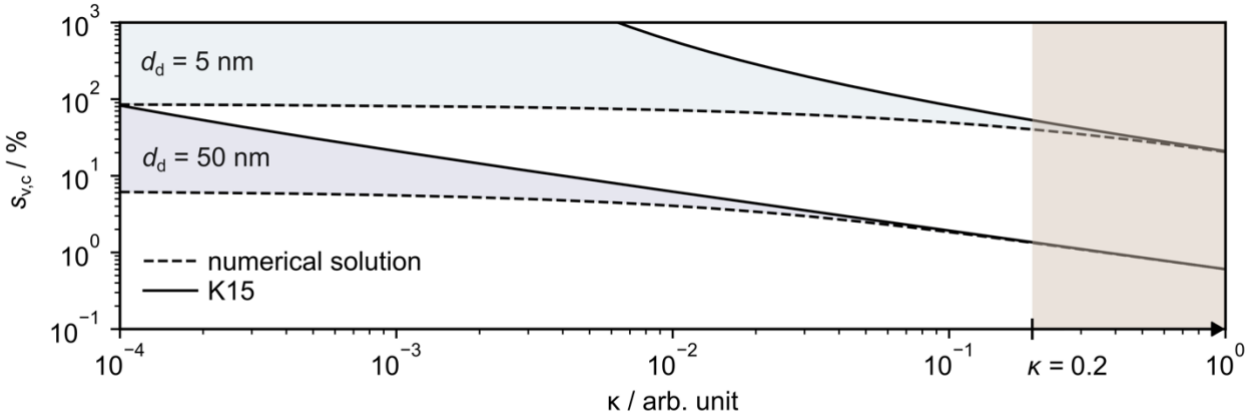

Figure S4: Comparison of numerical versus analytical treatment of *κ*-Köhler theory at *T* = 230 K.

In Fig. S4, we compare the analytical and numerical approaches to estimating $S_{\mathrm{v,c}}$. Estimates have been shown for two dry particle diameters, d_{d} = 5 nm and 50 nm, to highlight the size dependence. In summary, we find that the condition $\kappa > 0.2$ is valid (i.e., the numerical and analytical approximation agree to within ~ 1%) provided $d_{\mathrm{d}} \gtrsim 10$ nm. The approximation collapses for smaller dry particle diameters and overpredicts the numerical result by a factor ~1.3 and ~10 for $d_{\mathrm{d}} = 5$ nm and $d_{\mathrm{d}} = 1$ nm (not shown) respectively (at κ = 0.2). Therefore, for the purposes of this work, the analytical model is strictly applicable for particles that satisfy both $d_{\mathrm{d}} > 10$ nm *and* $\kappa > 0.2$. Whilst these conditions are met for the majority of the nvPM and ambient particles considered in K15, they are not met for smaller vPM particles. Therefore, we choose to apply the full numerical solution to evaluate $S_{\mathrm{v,c}}$ in our extended K15 model simulations, at the cost of a marginal decrease in computational efficiency.

S8 K15 model extension: microphysical term

To determine $n_{\mathrm{w}}^{(2)}(t)$, first we need to identify the temporal dependence of L_{w}. This is achieved by approximating the functional dependence of $\dot{n}_{\mathrm{w}}(t_0)$ as (Ford, 1998)

$$\dot{n}_{\mathrm{w}}(t_0) = \dot{n}_{\mathrm{w}}(t) e^{-\frac{t-t_0}{\tau_{\mathrm{act}}}}, \tag{S18}$$

where τ_{act} is the characteristic timescale of activation within the mixing plume. This prescribes that the largest contribution to $L_{\mathrm{w}}(t)$ occurs from droplet activation and growth within a narrow activation window $(t - t_0) \sim \tau_{\mathrm{act}}$, in a burst-like activation event. For additional justification on the form of the ansatz, the reader is directed to the original texts (Ford, 1998; Kärcher and Lohmann, 2003). Note that Eq. (S18) allows us to define the total number of activated particles in terms of the nucleation rate, $n_{\mathrm{w}}(t) = \dot{n}_{\mathrm{w}}(t)\tau_{\mathrm{act}}$. Hence, using this relation along with Eq. (S18), we can transform Eq. (25) (in the main text) as

$$L_{\mathrm{w}} = \frac{4\pi}{n_{\mathrm{w}}^{\mathrm{sat}} \upsilon} \frac{n_{\mathrm{w}}(t)}{\tau_{\mathrm{act}}} \int_0^{\infty} \mathrm{d}r_0 \frac{dn_{\mathrm{w}}}{dr_0} \int_{-\infty}^{t} e^{-\frac{t-t_0}{\tau_{\mathrm{act}}}} \mathrm{r}_{\mathrm{w}}^2(t, t_0) \dot{r}_{\mathrm{w}}(t, t_0)\, \mathrm{d}t_0, \tag{S19}$$

where we have used the ideal gas law to redefine the prefactor in terms of $n_{\mathrm{w}}^{\mathrm{sat}}$ and υ, the water vapor number density at water saturation and volume of a water molecule in supercooled water, respectively. The definition of the radial growth law, $\dot{r}_{\mathrm{w}}$, is described in more detail in SI S2. Critically, our definition of the radial growth law departs from the definition used in K15 and earlier work (Ford, 1998; Kärcher and Lohmann, 2003), as we have chosen to explicitly incorporate the Kelvin effect. This enables us to more accurately describe water uptake by the smaller vPM mode. For efficient computational models, it is preferable that the solutions to Eq. (S19) are analytic, which is only possible if both integrations can be solved analytically. Therefore, we will next outline several approaches to solving the integrations.

The outer integration takes place over the activated particle size distribution. Although this can be solved numerically, there are also several approximations that can be used to yield compact analytical solutions. In the K15 model, the authors replace this integral using the critical droplet radius, weighted by the available number concentration of each particle type, $\bar{r}_{\mathrm{w,c}}$. This approach assumes that all contributions made at time t_0 are from particles with the critical radius $r_{\mathrm{w,c}}$. However, as we have shown in Sect. 2.2 of the main text, particles with radii $r > r_{\mathrm{w,c}}$ are also able to activate. In other words, it is possible that this approach underestimates the mean activated particle radius at a given time t_0. We explore a replacement for the first integral by using the arithmetic mean particle radius over the truncated activated size distribution, which is then weighted by the available number concentration of each particle type. We denote this as $\tilde{r}_{\mathrm{w,c}}$. We will later show under which circumstances this approach provides better agreement with the numerical solution than the original K15 model approach.

Within the K15 model, the authors perform the inner integration by separating the integral into two cases (Kärcher and Lohmann, 2003). To explain the physical meaning of these cases, we first define the relaxation parameter, κ_{w}, as the ratio of the droplet activation and growth timescales, τ_{act} and τ_{gw} respectively,

$$\kappa_{\mathrm{w}} = \frac{\tau_{\mathrm{act}}}{\tau_{\mathrm{gw}}};\ \tau_{\mathrm{gw}} = \frac{1}{\left(\frac{\partial \ln r_{\mathrm{w}}}{\partial t}\right)} = \frac{r_{\mathrm{w}}(1 + b_2 r_{\mathrm{w}})}{A}, \tag{S20}$$

where the prefactor, A can either include or omit the Kelvin effect and is described in SI S2. This enables us to define the first case as the slow-growth regime, where particle activation dominates over droplet growth and $\kappa_{\mathrm{w}} < 1$. The second case is the fast-growth regime, where droplet growth dominates over particle activation and $\kappa_{\mathrm{w}} > 1$. These cases permit us to prescribe limiting behaviour in the droplet growth law, thereby eliminating the t-dependence in Eq. (S19). For a full description of this method, the reader is directed to Kärcher and Lohmann, 2003. When the Kelvin effect is not included in the growth law, analytical solutions for the inner integration can be determined in both the slow- and fast-growth regimes. On the other hand, incorporating the Kelvin effect within the radial growth law precludes an analytical approach, and the resulting expression can only be solved numerically. However, the slow-growth regime can still be solved analytically, and the solution is given by

$$L_w = \frac{4\pi \bar{r}_{\mathrm{w,c}}^3 n_{\mathrm{w}}(t)}{n_{\mathrm{w}}^{\mathrm{sat}} \tau_{\mathrm{gw}} \upsilon} (2\kappa_{\mathrm{w}}^2 + 2\kappa_{\mathrm{w}} + 1), \tag{S21}$$

including our earlier approximating regarding the outer integration. If the Kelvin effect is omitted, it is also possible to solve Eq. (S19) analytically for all growth regimes as described in Kärcher et al. (2006).

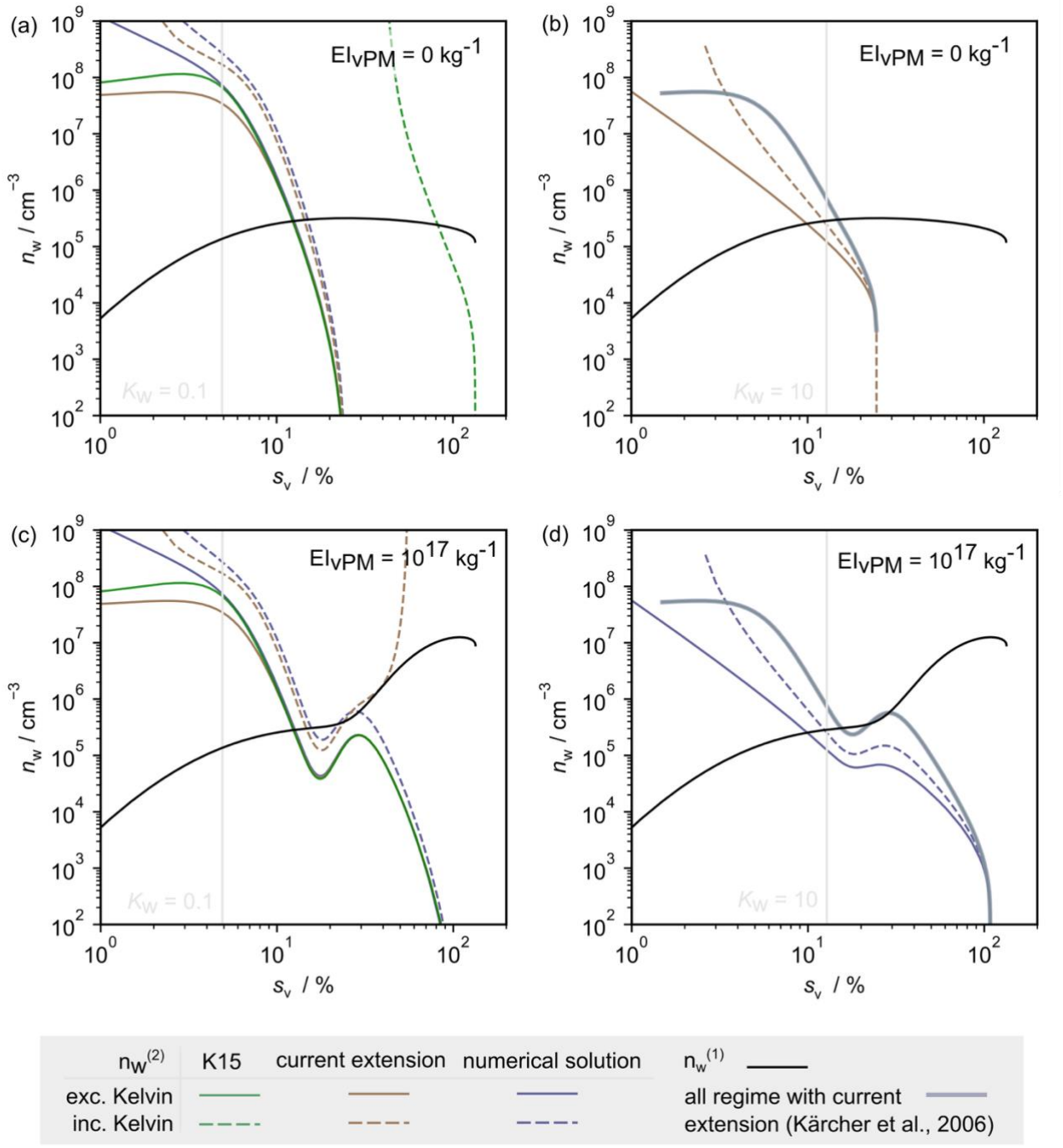

Figure S5: variation of $n_w^{(2)}$ and $n_w^{(1)}$ with increasing plume supersaturation for T_A = 215 K and G = 1.64 PaK^{-1} in the soot-rich regime (EI$_{nvPM}$ = 10^{15} kg^{-1}), using the particle properties for GMD, GSD and κ defined in Table of the main text. In panels (a) and (b), EI$_{vPM}$ = 0 kg^{-1} (as in the original K15 model) whereas in panels (c) and (d), EI$_{vPM}$ = 10^{17} kg^{-1}. In panels (a) and (c) $n_w^{(2)}$ has been computed for the *slow*-growth regime with inclusion (inc.) and exclusion (exc.) of the Kelvin effect. For each of these, the outer integral has been estimated using three approaches: solving numerically (thinner purple lines), using the B15 model (green lines) and using our extension (brown lines). In panels (b) and (d) $n_w^{(2)}$ has been computed for the *fast*-growth regime with inclusion (inc.) and exclusion (exc.) of the Kelvin effect. Also, results valid across all regimes have been plotted (thicker purple lines), excluding the Kelvin effect (Kärcher et al., 2006). In each case, the outer integral has been estimated using our extension. In panel (a/c) and (b/d), vertical lines have also been shown corresponding to $\kappa_w = 0.1$ and $\kappa_w = 10$ respectively, defining the approximate limits of applicability according to Eq. (S20).

In Fig. S5, we have demonstrated how $n_{\mathrm{w}}^{(1)}$ and $n_{\mathrm{w}}^{(2)}$ vary with plume supersaturation under typical contrail-forming conditions (T_{A} = 215 K, G = 1.64 PaK^{-1}). These have been estimated in the soot-rich regime (EI$_{\mathrm{nvPM}}$ = 10^{15} kg^{-1}) with and without vPM, using particle characteristics outlined in Table. 1 of the main text. In Fig. S5a, we show the variation of $n_{\mathrm{w}}^{(2)}$ deriving from the solutions for L_{w} in the slow-growth regime. We find that within its range of validity ($\kappa_{\mathrm{w}} < 0.1$), incorporating the Kelvin effect can have a pronounced impact on estimates for soot-rich conditions. In all cases, inclusion of the Kelvin effect acts to increase the effective number of contrail ice crystals, n_{i}. This is because inclusion of the Kelvin effect suppresses the radial growth of water droplets, see Eq. (S8). Moreover, the size-dependence of the Kelvin effect means that if the available particles are smaller, the effect will be more pronounced. This is illustrated in Fig. S5c, where the relative difference between the solid (exc. Kelvin effect) and dashed (inc. Kelvin effect) lines increases dramatically once vPM activation becomes dominant (for $s_{\mathrm{v}} > 30\%$) and $\tilde{r}_{\mathrm{w,c}}$ approaches $d_{\mathrm{g,vPM}}$. We can also use Fig. S5a to compare the various approaches to evaluating the outer integral. Taking the numerical approach as a benchmark, we find better agreement using our approach than the original K15 approach, provided the Kelvin effect is *included*. This is due to the exponential dependence in Eq. (7) of the main text, which is highly sensitive to the choice of mean activated particle radius ($\bar{r}_{\mathrm{w,c}}$ or $\tilde{r}_{\mathrm{w,c}}$). However, when the Kelvin effect is omitted, both approaches provide comparable results and here we choose to use the original K15 approach. Additionally, we find that when the vPM mode is included, it is no longer feasible to estimate $n_{\mathrm{w}}^{(2)}$ for the slow growth regime using the K15 approach with incorporation of the Kelvin effect. For this reason, there is no dashed green line shown in Fig. S5c.

In Fig. S5b and Fig. S5d, we show fast-growth regime solutions that include our outer integral extension with and without inclusion of the Kelvin effect. Inclusion of the Kelvin effect is relatively less impactful in the fast-growth regime solutions compared to the corresponding slow-growth solutions. This aligns with intuition, as when the microphysical term is dominated by droplet growth (as opposed to activation), the initial aerosol properties become less important (Kärcher et al., 2006). In Fig. S5b and Fig. S5d we also show the solution originally derived in Kärcher et al. (2006) that is valid across both regimes (albeit without inclusion of the Kelvin effect) and illustrate its consistency with the slow- and fast-growth solutions under their respective ranges of validity. Critically, when vPM particles are incorporated in the model – see Fig. S5c and Fig. S5d – the intersection of $n_{\mathrm{w}}^{(1)}$ and $n_{\mathrm{w}}^{(2)}$ occurs for $\kappa_{\mathrm{w}} > 10$ and therefore should only be described using solutions for the fast-growth regime. For this reason, we have chosen to adopt the result outlined by Kärcher et al. (2006), which is applicable across all growth regimes. In doing so, we are forced to omit the Kelvin effect and our updated approach for estimating

S9 Model sensitivity to number of vPM modes

In our model, we assume that all vPM particles have identical chemical composition, which is encompassed by the prescribed total hygroscopicity parameter, κ. Due to the nature of vapour condensation in the nascent plume, it is possible that the vPM mode may be distributed into several particle types with different chemical composition (Cantin et al., 2024; Yu et al., 1999). To explore the impact of the aforementioned model assumption, we have divided the vPM mode into two distinct modes: vPM-1 and vPM-2, see Table. S1. This is consistent with experimental measurements of chemi-ions, which show that positive chemi-ions (vPM-2) are mostly comprised of protonated organic material (Kiendler et al., 2000b; Sorokin and Arnold, 2006) while negative chemi-ions (vPM-1) are mostly comprised of deprotonated acidic moieties (derivatives of nitric and sulphuric acid) (Kiendler et al., 2000a). As in our original approach, we can effectively modify the chemical composition of vPM-2 by altering the value of κ associated with it. Finally, we have assumed that the concentrations of vPM-1 and vPM-2 are equivalent ($EI_{vPM\text{-}1} = EI_{vPM\text{-}2}$), in line with in-situ observations (Haverkamp et al., 2004).

Table. S1: particle properties for simulations comprising two vPM modes: vPM-1 and vPM-2.

Mode properties	EI / kg^{-1}	d_g / nm	$\boldsymbol{\sigma_g}$ / no units	κ / no units
Plume vPM-1	5×10^{16}	2.5	1.3	0.5 (H_2SO_4)
Plume vPM-2	5×10^{16}	2.5	1.3	0 – 0.5 (organic material)
nvPM	$10^{12} – 10^{15}$	35	2.0	0.005
ambient	600 cm^{-3}	30	2.2	0.5

As anticipated, we find that when the composition of vPM-2 is purely sulphuric acid, results are equivalent to assuming a single vPM mode as shown in Fig. 7 of the main text (see Fig. S6). When dividing the vPM mode into a mode comprising sulphuric acid and another comprising organic material, AEI_{ice} estimates depend on the chemical composition of vPM-2. As the hygroscopicity of the vPM-2 mode is reduced, a reduced proportion of these particles activate to form water droplets (and freeze to form ice crystals). Ultimately, when the hygroscopicity of this mode has been reduced below $\kappa = 0.01$, AEI_{ice} derives exclusively from vPM-1. Therefore, the effective result is a reduction in AEI_{ice}. Notably, the effect of dividing the vPM mode in two distinct modes with different values of κ is similar to assuming a single mode with a lower mean value of κ. Therefore, we assert that our sensitivity analysis in Fig. 9 of the main text is sufficient to cover the physical possibility of a more complicated, multicomponent vPM mode. Additionally (as demonstrated in Fig. S6), our model is sufficiently flexible to incorporate additional vPM complexity when the properties of this mode are experimentally grounded.

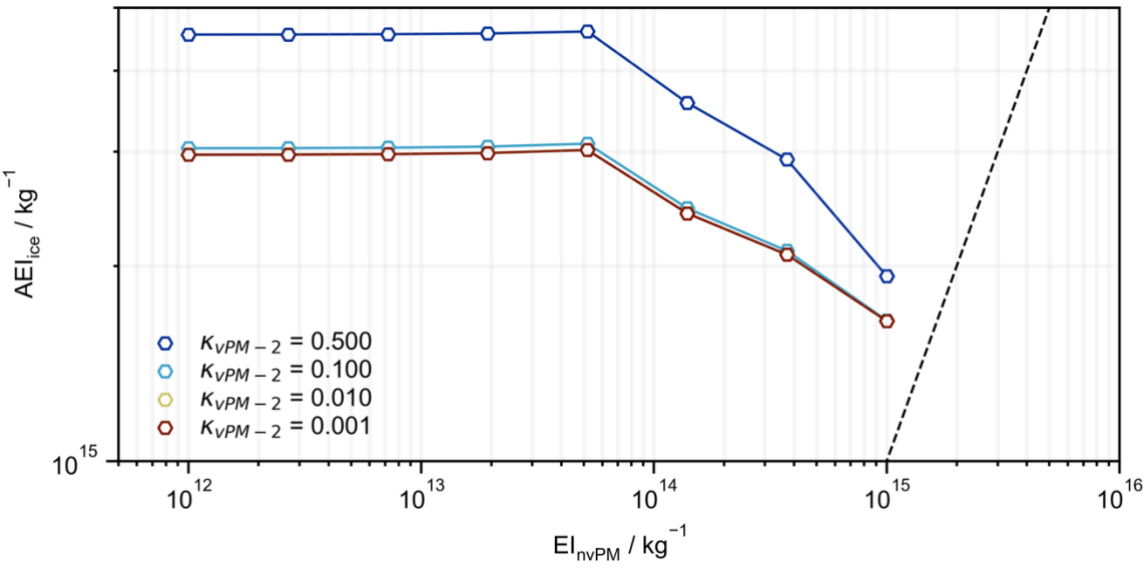

Figure S6: AEI_{ice} sensitivity to EI_{nvPM} and the chemical composition of vPM-2. Note, due to the large increase in the number of tracked size bins when incorporating the additional vPM mode, estimates at large values of EI_{nvPM} (> 10^{15} kg^{-1}) could not be obtained.

S10 Model sensitivity to nvPM particle size

The properties of aircraft nvPM particles can be investigated by performing ground-based measurements behind turbofan engines (Saffaripour et al., 2020). Primary particle size distribution characteristics are typically determined offline, using samples collected for Transmission Electron Microscopy (TEM). Image analysis software is then used to extract information from individual samples, including aggregate scaling properties, the geometric mean primary particle diameter ($d^{(p)}_{g,nvPM}$) and geometric standard deviation ($\sigma^{(p)}_{g,nvPM}$) (Sipkens et al., 2023). Using Table. 2 in Saffaripour et al. (2020), we have selected and/or extracted relevant primary particle size distribution characteristics for samples collected at 100% thrust from turbofan engines burning Jet A-1, which were obtained from TEM images. To that end, using data from (a) Liati et al. (2014): $d^{(p)}_{g,nvPM}$ = 17.4 nm, $\sigma^{(p)}_{g,nvPM}$ = 1.54; (b) Marhaba et al. (2019): $d^{(p)}_{g,nvPM}$ = 13.5 nm, $\sigma^{(p)}_{g,nvPM}$ = 1.50 and (c) Delhaye et al. (2017): $d^{(p)}_{g,nvPM}$ = 16.1 nm, $\sigma^{(p)}_{g,nvPM}$ = 1.50, we estimate average primary particle size distribution characteristics $d^{(p)}_{g,nvPM}$ = 15.7 ± 1.6 nm and $\sigma^{(p)}_{g,nvPM}$ = 1.50 ± 0.02. Given our choice of geometric mean aggregate particle diameter ($d^{(a)}_{g,nvPM}$ = 35 nm), the ratio of mean primary-to-aggregate particle sizes is XR = 0.45, which is similar to the baseline value XR = 0.41 used in Yu et al. (2024). However, here we choose to discriminate between primary or aggregate particle size distribution characteristics using the superscript (p)/(a) as both the GMD *and* the GSD are modified.

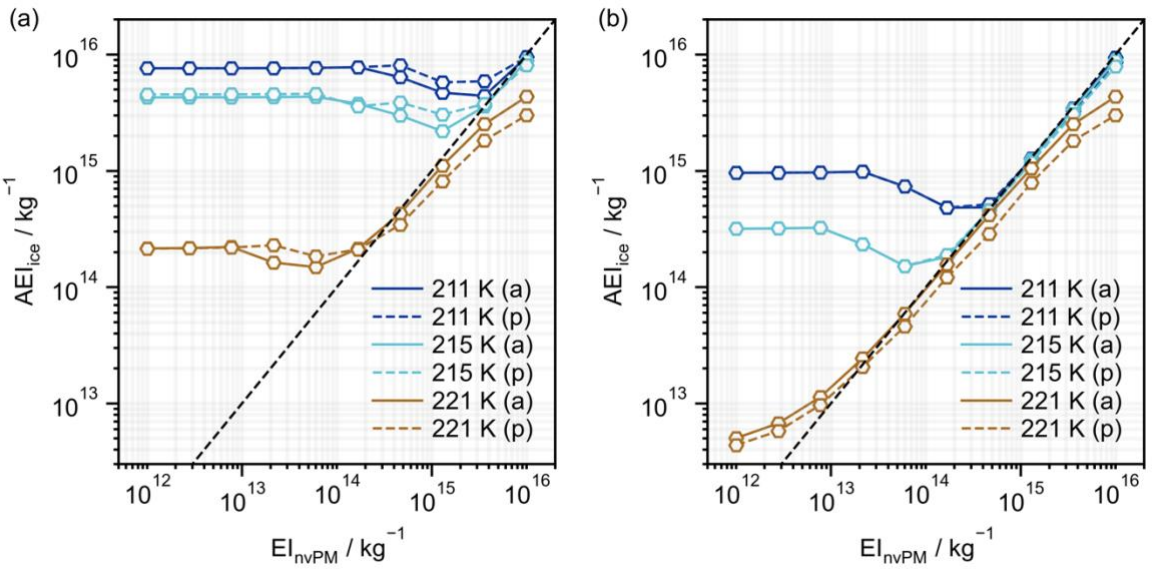

Figure S7: apparent ice emission index at 230 K (hexagonal markers) and its dependence on T_A and EI_{nvPM} for (a) sulphur-rich and (b) organic-rich volatile particles. The impact of assuming aggregate "(a)" or primary "(p)" particle size distribution characteristics, GMD and GSD of (35 nm, 2.0) and (15.7, 1.5) respectively, is shown.

Fig. S7 shows AEI_{ice} sensitivity to T_A, EI_{nvPM} and the choice of either nvPM primary particles or aggregates, using (a) sulphur-rich and (b) organic-rich vPM properties as described in Sect. 3.4 of the main text. For temperatures close to T_{SAC}, AEI_{ice} is reduced if most droplets are formed via nvPM. This is because for a given plume supersaturation, more nvPM aggregate particles are able to activate than nvPM primary particles, due to the larger GMD and GSD. Therefore, when $EI_{nvPM} = 10^{16}$ – which precludes substantial vPM activation in the case of both sulphur- and organic-rich vPM - AEI_{ice} is reduced by 30% when using nvPM primary particles compared to aggregates. For sulphur-rich conditions, as the minimum is approached from high EI_{nvPM} which implies competition between vPM and nvPM, AEI_{ice} is increased by up to 40% when using nvPM primary particles compared to aggregates. Again, this occurs because fewer nvPM primary particles are able to activate at a given supersaturation compared to aggregates, so the more numerous vPM mode is able to compete for available water vapour at a higher EI_{nvPM}.

Overall, we find that upon changing our description from nvPM aggregates to primary particles: (i) if most water droplets form via nvPM, AEI_{ice} is reduced as a smaller proportion of the nvPM size distribution can activate and (ii) if a large proportion of droplets form via vPM (i.e., the minimum in Fig. S7), AEI_{ice} is increased as nvPM provides less competition for available supersaturation and (iii) for sulphur-rich vPM, (i) + (ii) lead to an effective translation of the aggregate profiles in Fig. S7 (a) towards increased EI_{nvPM}. Each of these results is qualitatively consistent with the findings in Yu et al. (2024).

S11 Pyrcel uncertainty estimate

In pyrcel, changing the number of size bins for a given mode changes the discretization of particle diameters. Given the parameterization for activation is highly sensitive to particle diameter (see Eq. (9) in the main text), small adjustments to these values can therefore impact activated particle number concentrations and AEI_{ice}. During our analyses, we noticed that AEI_{ice} was more sensitive to the prescribed number of size bins for vPM than for nvPM. We suggest that this is likely a consequence of two factors. Firstly, $d_{g,vPM}$ is smaller than $d_{g,nvPM}$ (see Table. 1 in the main text) and activated number concentrations are increasingly sensitive to smaller particle diameters (see Fig. 2b in the main text). Secondly, the droplet and ice (see Fig. S8) particle size distributions for nvPM and vPM have different forms. For nvPM, the maximum in the ice particle size distribution is distinctly separated from the minimum diameter of activation. However, for vPM, the maximum in the ice particle size distribution *is* equivalent to the minimum diameter of activation. As a result, small changes in the quantization of size bins (that modify the minimum diameter of activation) have a large effect on the number concentration of vPM-derived ice crystals but not on the concentration of nvPM-derived ice crystals.

For this reason, we decided to interrogate model sensitivity to the prescribed number of (n)vPM size bins. We chose to investigate the sensitivity under soot-poor conditions ($EI_{nvPM} = 10^{12}$ kg^{-1}) as this represents the point at which AEI_{ice} is maximally sensitive to vPM. Therefore, we can use the sensitivity at this point to derive maximum uncertainties. Accordingly, simulations were performed using a sulphur-rich plume vPM mode (according to Table. 1 in the main text), $T_A = 215$ K and $EI_{nvPM} = 10^{12}$ kg^{-1}. When varying the number of vPM size bins, other size bin numbers were fixed at 50. Model sensitivity to the number of vPM size bins is shown in Fig. S9.

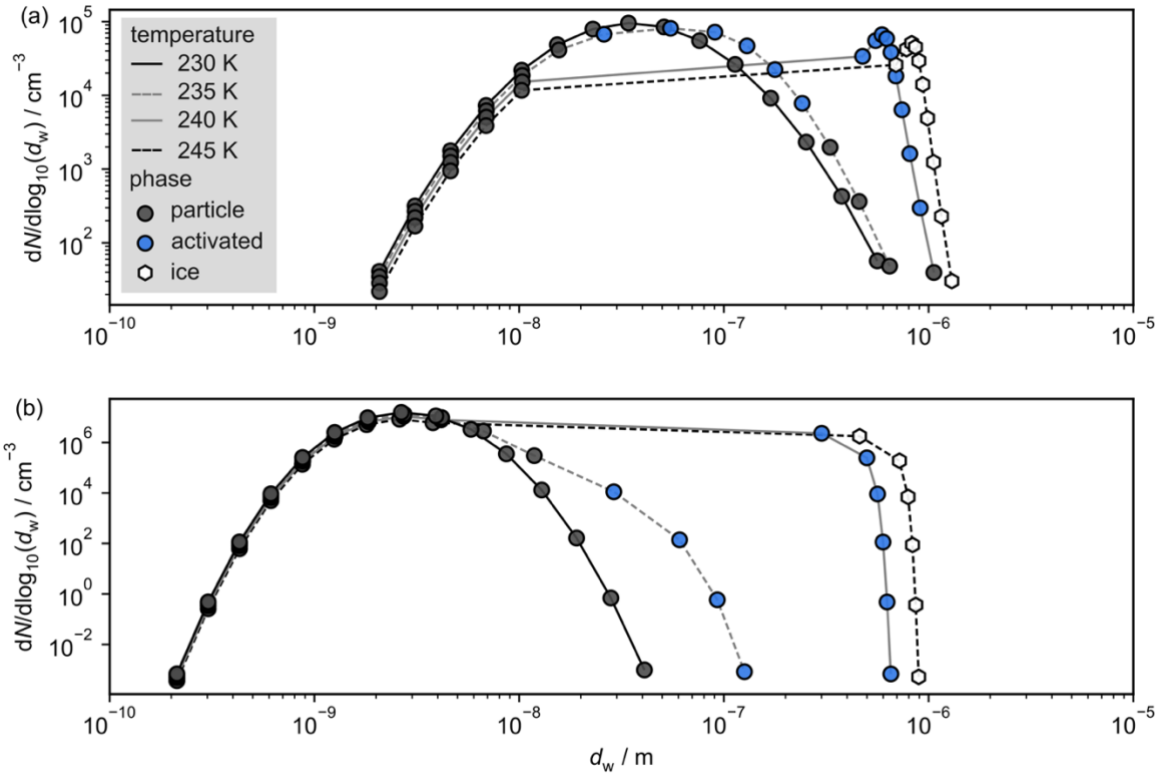

Figure S8: particle size distributions for (a) nvPM and (b) vPM illustrative of typical contrail mixing behaviour. The particle size distributions have been shown at four different temperatures during plume evolution and the phase (solid/liquid aerosol, liquid droplet, ice crystal) of each bin has been indicated using a different marker.

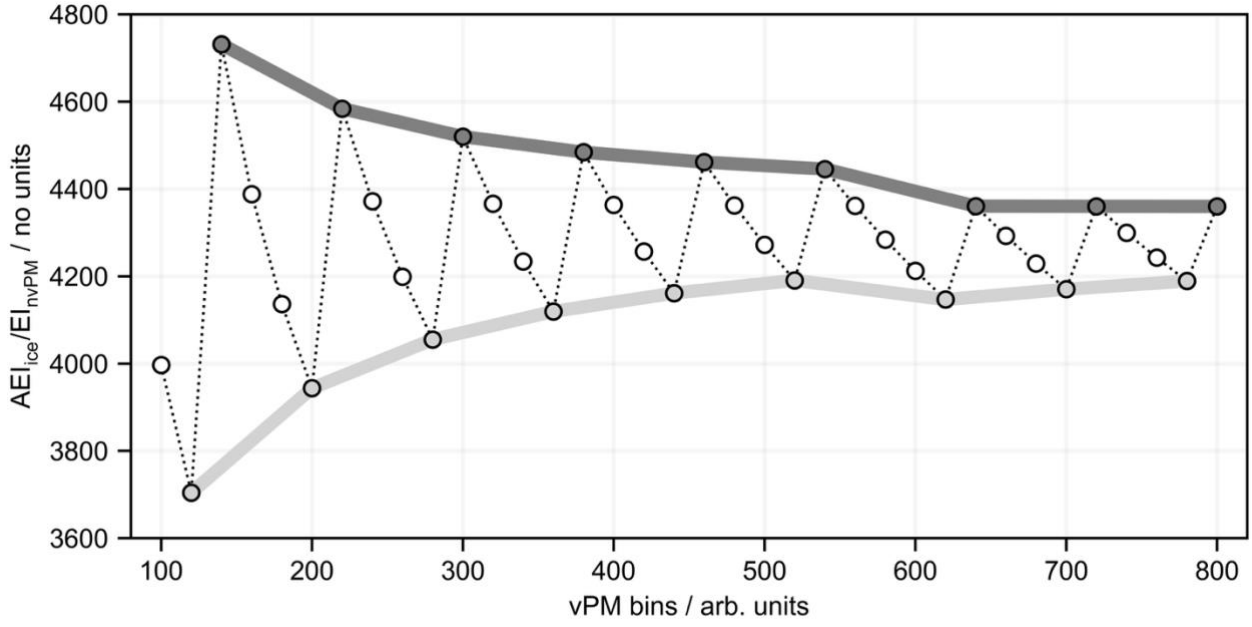

Figure S9: AEI_{ice} sensitivity (normalised by $EI_{nvPM} = 10^{12}$ kg^{-1}) to the number of size bins prescribed for vPM. An envelope is drawn to constrain maximum errors associated with each vPM bin number.

Previously, we found that AEI_{ice} estimates were largely insensitive to the number of prescribed nvPM size bins. However, for vPM, we find that AEI_{ice} estimates converge with increasing numbers of size bins. By enveloping these estimates, we find that errors range from -10% to +9% for 150 size bins, which is the typical number used in our model simulations. Therefore, this represents the maximum uncertainty in our AEI_{ice} estimates.

S12 Upper tropospheric ambient temperatures

Meteorological and Automatic Dependent Surveillance-Broadcast (ADS-B) data were obtained from Spire Aviation (Spire Aviation, 2024) and ECMWF respectively for the date 01/01/2019. The purpose of this analysis is to assess the upper tropospheric lapse rate at typical contrail-forming altitudes and comment on implications for temperature-based contrail avoidance.

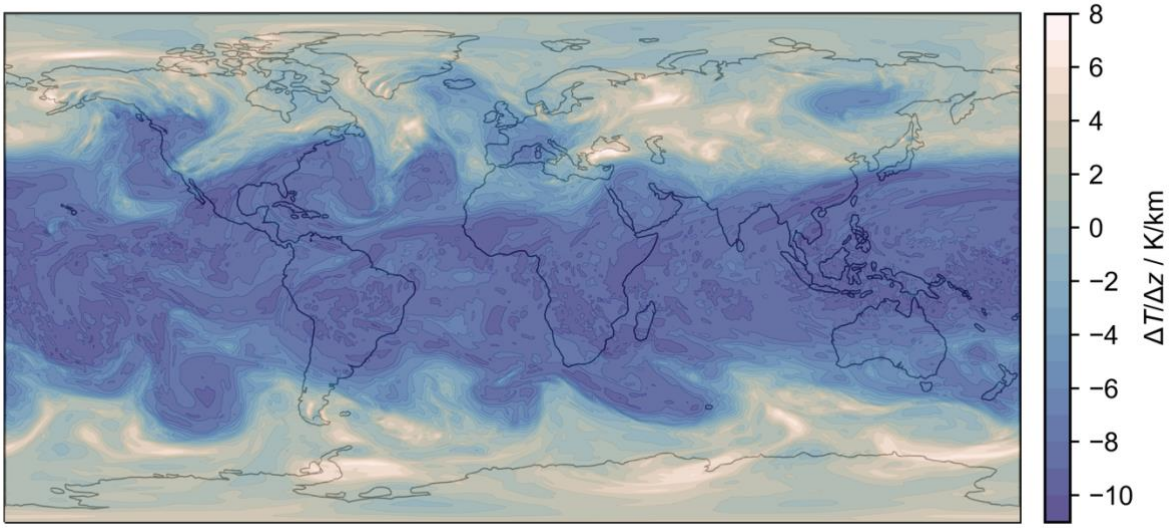

Figure S10: upper tropospheric lapse rate ($\Delta T/\Delta z$) at the mean contrail-forming altitude obtained for flight waypoints satisfying the SAC using the Spire and ECMWF datasets for 01/01/2019.

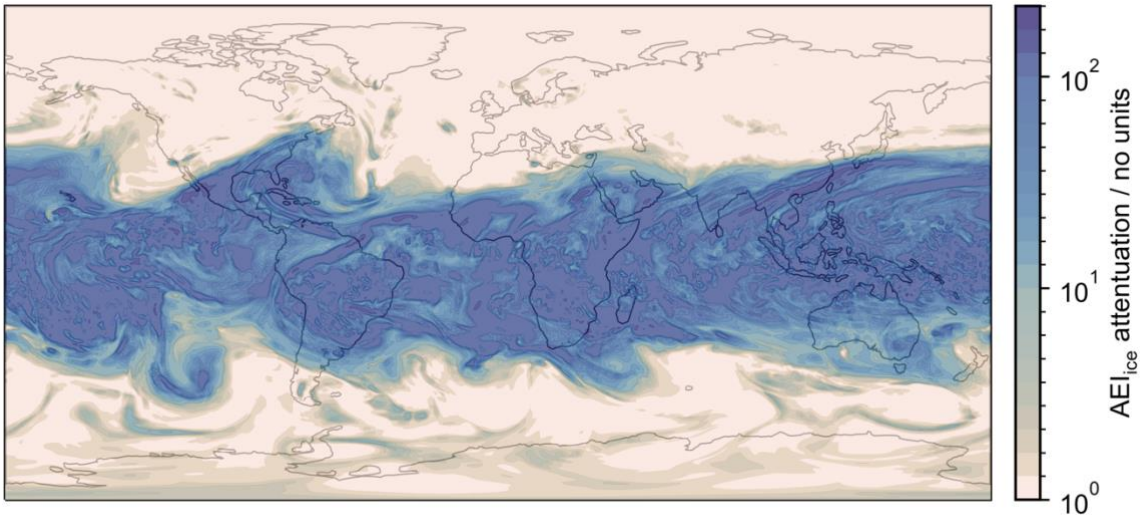

Figure S11: attenuation in AEI_{ice} achieved for soot-poor conditions ($EI_{nvPM} = 10^{12}$ kg^{-1}) with deviations of ± 10 flight levels from the mean contrail-forming altitude.

Fig. S10 shows how the upper tropospheric lapse rate ($\Delta T/\Delta z$) calculated at the mean contrail-forming altitude (contrail waypoints that satisfy the SAC) varies as a function of longitude and latitude. We find that within the tropics (± 23.5°), the lapse rate is approximately – (8 ± 1) K/km; the temperature increases with a decrease in altitude. Here, ambient temperature changes of ~2 K are possible by reducing cruise altitudes by ± 10 flight levels (1000 ft). By contrast, in the extratropical regions, the lapse rate exhibits greater variation and can be positive.

In Fig. 9 of the main text, we presented the dependence of AEI_{ice} on ambient temperature for various emissions scenarios. Using these data with the information in Fig. S10, we can estimate the reduction in AEI_{ice} (without sublimation losses) that could be achieved by altering flight altitudes by ± 10 flight levels. For the purpose of this discussion, we have focussed on the soot-poor regime, where the greatest attenuation of the apparent emission index of ice ($AEI_{ice,\ unadjusted}$ / $AEI_{ice,\ with\ altitude\ adjustment}$) is possible (see Fig. 9 of the main text). We find that attenuations exceeding 100 are achievable in the tropics by reducing flight altitudes by 10 flight levels. Smaller attenuations are achievable in the extratropical regions as the ambient temperature at the mean contrail-forming altitude is cooler.

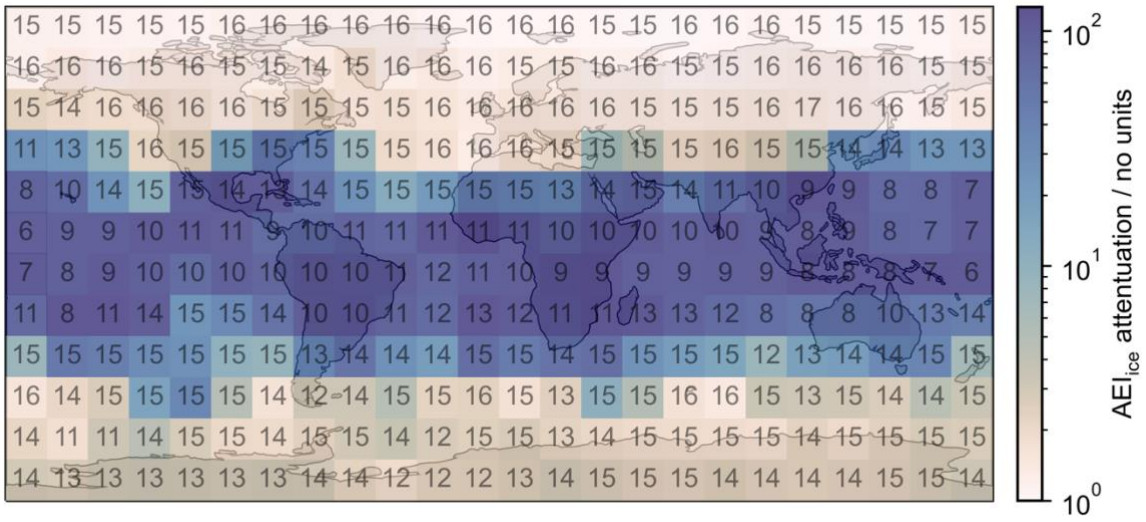

Figure S12: attenuation in AEI_{ice} as in Fig. S11. The value of $\log_{10}(AEI_{ice})$ at the mean contrail-forming altitude has also been marked on each grid cell for reference.

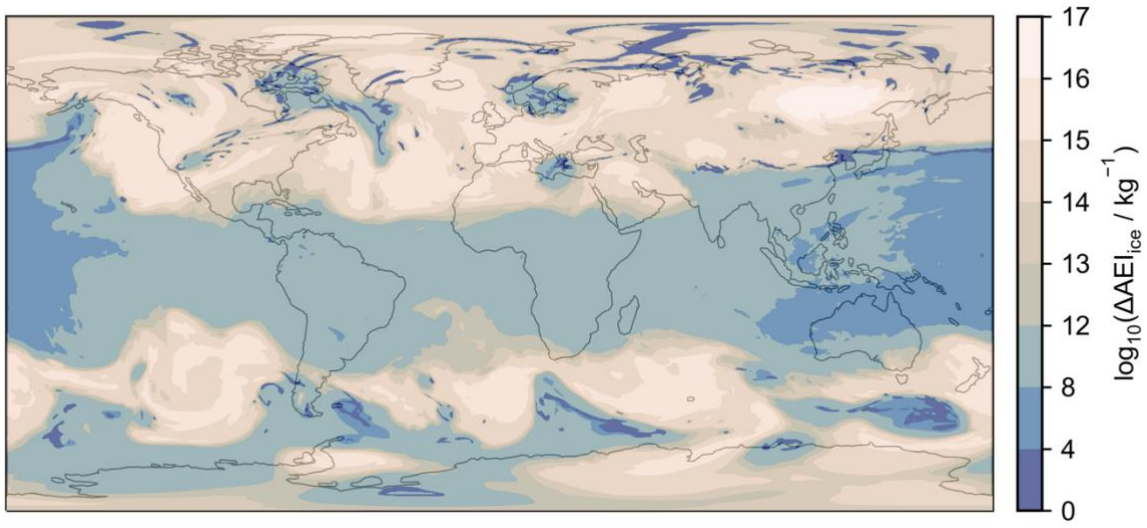

Figure S13: absolute reduction in AEI_{ice} achieved for soot-poor conditions ($EI_{nvPM} = 10^{12}$ kg^{-1}) with deviations of ± 10 flight levels from the mean contrail-forming altitude.

Although larger attenuations are achieved in the tropics compared to the extratropical regions, warmer ambient temperatures mean that absolute AEI_{ice} emissions at the mean contrail-forming altitude are typically lower, see Fig. S13. Absolute reductions in AEI_{ice} ($AEI_{ice,\ unadjusted}$ - $AEI_{ice,\ with\ altitude\ adjustment}$) therefore provide a more suitable metric for targeting the most warming contrails, which are associated with larger AEI_{ice} (Teoh et al., 2022). To that end, we find that the largest absolute reductions in AEI_{ice} are found in the northern midlatitudes (~ 30° - 60°). This covers some of the densest regions of global air traffic, including Europe and North America (Teoh et al., 2023). Moreover, the above analysis was performed using meteorological data during winter in the Northern Hemisphere. During the summer months, upper tropospheric temperatures in the Northern Hemisphere are warmer so the potential for temperature-based mitigation in this region is improved. Overall, avoiding cooler regions of the atmosphere may provide an alternative strategy for contrail mitigation.

References

Spire Aviation: https://spire.com/wiki/how-ads-b-has-shaped-the-modern-aviation-industry/, last access: 19 December 2024.

Baumgartner, M., Rolf, C., Grooß, J.-U., Schneider, J., Schorr, T., Möhler, O., Spichtinger, P., and Krämer, M.: New investigations on homogeneous ice nucleation: the effects of water activity and water saturation formulations, Atmospheric Chemistry and Physics, 22, 65–91, https://doi.org/10.5194/acp-22-65-2022, 2022.

Bier, A., Unterstrasser, S., and Vancassel, X.: Box model trajectory studies of contrail formation using a particle-based cloud microphysics scheme, Atmos. Chem. Phys., 22, 823–845, https://doi.org/10.5194/acp-22-823-2022, 2022.

Cantin, S., Chouak, M., and Garnier, F.: Eulerian–Lagrangian CFD-microphysics modeling of aircraft-emitted aerosol formation at ground-level, Aerosol Science and Technology, 58, 1347–1370, https://doi.org/10.1080/02786826.2024.2395940, 2024.

Delhaye, D., Ouf, F.-X., Ferry, D., Ortega, I. K., Penanhoat, O., Peillon, S., Salm, F., Vancassel, X., Focsa, C., Irimiea, C., Harivel, N., Perez, B., Quinton, E., Yon, J., and Gaffie, D.: The MERMOSE project: Characterization of particulate matter emissions of a commercial aircraft engine, Journal of Aerosol Science, 105, 48–63, https://doi.org/10.1016/j.jaerosci.2016.11.018, 2017.

Ford, I.: Ice nucleation in jet aircraft exhaust plumes, in: Pollution from aircraft emissions in the North Atlantic flight corridor (POLINAT 2): final report, Office for Official Publ. of the European Communities, Luxembourg, 269–287, 1998.

Haverkamp, H., Wilhelm, S., Sorokin, A., and Arnold, F.: Positive and negative ion measurements in jet aircraft engine exhaust: concentrations, sizes and implications for aerosol formation, Atmospheric Environment, 38, 2879–2884, https://doi.org/10.1016/j.atmosenv.2004.02.028, 2004.

Kärcher, B. and Lohmann, U.: A parameterization of cirrus cloud formation: Heterogeneous freezing, Journal of Geophysical Research: Atmospheres, 108, https://doi.org/10.1029/2002JD003220, 2003.

Kärcher, B., Hendricks, J., and Lohmann, U.: Physically based parameterization of cirrus cloud formation for use in global atmospheric models, Journal of Geophysical Research: Atmospheres, 111, https://doi.org/10.1029/2005JD006219, 2006.

Kärcher, B., Burkhardt, U., Bier, A., Bock, L., and Ford, I. J.: The microphysical pathway to contrail formation, JGR Atmospheres, 120, 7893–7927, https://doi.org/10.1002/2015JD023491, 2015.

Kiendler, A., Aberle, S., and Arnold, F.: Negative chemiions formed in jet fuel combustion: new insights from jet engine and laboratory measurements using a quadrupole ion trap mass spectrometer apparatus, Atmospheric Environment, 34, 2623–2632, https://doi.org/10.1016/s1352-2310(99)00475-6, 2000a.

Kiendler, A., Aberle, S., and Arnold, F.: Positive ion chemistry in the exhaust plumes of an air craft jet engine and a burner: investigations with a quadrupole ion trap mass spectrometer, Atmospheric Environment, 34, 4787–4793, https://doi.org/10.1016/s1352-2310(00)00253-3, 2000b.

Koop, T., Luo, B., Tsias, A., and Peter, T.: Water activity as the determinant for homogeneous ice nucleation in aqueous solutions, Nature, 406, 611–614, https://doi.org/10.1038/35020537, 2000.

Lewellen, D. C.: A Large-Eddy Simulation Study of Contrail Ice Number Formation, Journal of the Atmospheric Sciences, 77, 2585–2604, https://doi.org/10.1175/JAS-D-19-0322.1, 2020.

Liati, A., Brem, B. T., Durdina, L., Vögtli, M., Arroyo Rojas Dasilva, Y., Dimopoulos Eggenschwiler, P., and Wang, J.: Electron Microscopic Study of Soot Particulate Matter Emissions from Aircraft Turbine Engines, Environ. Sci. Technol., 48, 10975–10983, https://doi.org/10.1021/es501809b, 2014.

Marcolli, C.: Technical note: Fundamental aspects of ice nucleation via pore condensation and freezing including Laplace pressure and growth into macroscopic ice, Atmos. Chem. Phys., 20, 3209–3230, https://doi.org/10.5194/acp-20-3209-2020, 2020.

Marhaba, I., Ferry, D., Laffon, C., Regier, T. Z., Ouf, F.-X., and Parent, P.: Aircraft and MiniCAST soot at the nanoscale, Combustion and Flame, 204, 278–289, https://doi.org/10.1016/j.combustflame.2019.03.018, 2019.

Murray, B. J., Broadley, S. L., Wilson, T. W., Bull, S. J., Wills, R. H., Christenson, H. K., and Murray, E. J.: Kinetics of the homogeneous freezing of water, Phys. Chem. Chem. Phys., 12, 10380–10387, https://doi.org/10.1039/C003297B, 2010.

Murray, B. J., O'Sullivan, D., Atkinson, J. D., and Webb, M. E.: Ice nucleation by particles immersed in supercooled cloud droplets, Chem. Soc. Rev., 41, 6519, https://doi.org/10.1039/c2cs35200a, 2012.

Petters, M. D. and Kreidenweis, S. M.: A single parameter representation of hygroscopic growth and cloud condensation nucleus activity, Atmospheric Chemistry and Physics, 7, 1961–1971, https://doi.org/10.5194/acp-7-1961-2007, 2007.

Pruppacher, H. R. and Klett, J. D.: Microphysics of clouds and precipitation, 2nd ed., Springer Dordrecht, Dordrecht, 2010.

Rogers, R. R. and Yau, M. K.: A short course in cloud physics, Third edition., Butterworth-Heinemann, Burlington, Massachusetts, 1 pp., 1996.

Saffaripour, M., Thomson, K. A., Smallwood, G. J., and Lobo, P.: A review on the morphological properties of non-volatile particulate matter emissions from aircraft turbine engines, Journal of Aerosol Science, 139, 105467, https://doi.org/10.1016/j.jaerosci.2019.105467, 2020.

Seinfeld, J. H. and Pandis, S. N.: Atmospheric chemistry and physics: from air pollution to climate change, 3rd ed., John Wiley & Sons, Inc, Hoboken, New Jersey, 2016.

Sipkens, T. A., Boies, A., Corbin, J. C., Chakrabarty, R. K., Olfert, J., and Rogak, S. N.: Overview of methods to characterize the mass, size, and morphology of soot, Journal of Aerosol Science, 173, 106211, https://doi.org/10.1016/j.jaerosci.2023.106211, 2023.

Sorokin, A. and Arnold, F.: Organic positive ions in aircraft gas-turbine engine exhaust, Atmospheric Environment, 40, 6077–6087, https://doi.org/10.1016/j.atmosenv.2006.05.038, 2006.

Teoh, R., Schumann, U., Gryspeerdt, E., Shapiro, M., Molloy, J., Koudis, G., Voigt, C., and Stettler, M. E. J.: Aviation contrail climate effects in the North Atlantic from 2016 to 2021, Atmos. Chem. Phys., 22, 10919–10935, https://doi.org/10.5194/acp-22-10919-2022, 2022.

Teoh, R., Engberg, Z., Shapiro, M., Dray, L., and Stettler, M.: A high-resolution Global Aviation emissions Inventory based on ADS-B (GAIA) for 2019–2021, https://doi.org/10.5194/egusphere-2023-724, 1 June 2023.

Vignati, E., Wilson, J., and Stier, P.: M7: An efficient size-resolved aerosol microphysics module for large-scale aerosol transport models, Journal of Geophysical Research: Atmospheres, 109, https://doi.org/10.1029/2003JD004485, 2004.

Yu, F., Turco, R. P., and Kärcher, B.: The possible role of organics in the formation and evolution of ultrafine aircraft particles, J. Geophys. Res., 104, 4079–4087, https://doi.org/10.1029/1998JD200062, 1999.

Yu, F., Kärcher, B., and Anderson, B. E.: Revisiting Contrail Ice Formation: Impact of Primary Soot Particle Sizes and Contribution of Volatile Particles, Environ. Sci. Technol., 58, 17650–17660, https://doi.org/10.1021/acs.est.4c04340, 2024.

Zhang, K., O'Donnell, D., Kazil, J., Stier, P., Kinne, S., Lohmann, U., Ferrachat, S., Croft, B., Quaas, J., Wan, H., Rast, S., and Feichter, J.: The global aerosol-climate model ECHAM-HAM, version 2: sensitivity to improvements in process representations, Atmospheric Chemistry and Physics, 12, 8911–8949, https://doi.org/10.5194/acp-12-8911-2012, 2012.